THE UNIVERSITY OF CALGARY

Creeping Flow Through Corrugated Tubes

by

Lutfoun Tahera Khanam

A THESIS

SUBMITTED TO THE FACULTY OF GRADUATE STUDIES

IN PARTIAL FULFILLMENT OF THE REQUIREMENTS FOR THE

DEGREE OF

MASTER OF ENGINEERING

DEPARTMENT OF CHEMICAL AND PETROLEUM ENGINEERING

CALGARY, ALBERTA

JANUARY, 1995

THE UNIVERSITY OF CALGARY

FACULTY OF GRADUATE STUDIES

The undersigned certify that they have read, and recommend to the Faculty of Graduate Studies for acceptance, a thesis entitled, "**Creeping Flow Through Corrugated Tubes**", submitted by **Lutfoun Tahera Khanam** in partial fulfillment of the requirements for the degree of Master of Engineering .

Ayodeji Jeje

Dr. A.A. Jeje (Supervisor)
Department of Chemical and
Petroleum Engineering

Robert A. Heidemann

Dr. R.A. Heidemann
Department of Chemical and
Petroleum Engineering

Richard D. Rowe

Dr. R.D. Rowe
Department of Mechanical Engineering

Date January 30, 1995

ABSTRACT

The dynamics of an incompressible fluid slowly flowing through internally corrugated circular tubes were studied experimentally and through numerical simulation. The corrugations involved step changes in diameter along a tube. Velocity profiles, pressure gradients in the tube and the streamline patterns inside the cavities were determined or observed. Hydrogen bubbles and fiber optics were employed for flow visualization. The flow rate of a highly viscous glycerine mixture with water was maintained in the creeping (Re < 2) regime.

Velocity profiles calculated through solving the stream function - vorticity transport equations showed spatial oscillations through different planes over a cycle of the corrugation. Configurations with wider cavities showed the maximum deviations from the parabolic profile through a tube of the same diameter as the narrower segment along the flow path. The results were qualitatively but not quantitatively similar to published experimental results to suggest an incomplete resolution of some issues in the numerical simulation. Calculated pressure drops show drag reduction relative to a smooth tube but the effect was not as dramatic compared to experimental measurements. For the latter, configurations with cavity aspect ratio (width/depth) of 0.5-0.6 and ridge to recess width ratios of ~ 1 showed the highest drag reductions; up to 30%. Both the calculated streamlines and those observed through streak photography of tiny hydrogen bubbles have similar contours but the calculated ones were more symmetric. The actual flows reveal irreversibility through asymmetry of streamlines.

ACKNOWLEDGEMENTS

I wish to express my sincere gratitude and thanks to Dr. A.A. Jeje, not only for his valuable guidance, encouragement, and support during the thesis work but also for sharing frequently his wisdom.. His continuous advice and invaluable suggestions all these years covered matters beyond the borders of fluid dynamics and are sincerely appreciated.

I also would like to thank Dr. R.A. Heidemann for giving me the opportunity to study at the University of Calgary.

I wish to express my appreciation to the members of the examining committee for their invaluable comments.

I would like to thank the Chemical Engineering technical staff, especially Adolf Kohl and Vince Krauss for their assistance in the design and construction of the experimental apparatus.

I also thank Rob Scorey, Michael Grigg and Bruce Miles for their technical help during the experimental work.

Manjit Singh, of the Electrical Engineering Department for his help in preparing the photographs for the thesis.

I would like to thank Dr. Doug Phillips and Dr. Paul Wellings, of the Academic Computing Services for their help regarding the use of the AIX computing system.

I would like to thank Canadian International Development Agency for their financial help.

I am especially indebted to my husband, Muqeem, and daughter, Tanziyah, for their love, understanding and companionship during these years. They shared with me the moment of joy and happiness, and also the moments of frustration, agony and stress which comes with the research work.

TABLE OF CONTENTS

LIST OF TABLES

LIST OF FIGURES

NOMENCLATURE

Symbol	Definition
a	radial distance to the ridge, m
b	radial distance to the mouth of the cavity, m
B	ball constant
D	diameter of the narrower tube segment, m
f	friction factor (Equation (5.3))
L	length of the measured distance, m
P	pressure, kPa
r	radial distance, m
R	radius of the narrower segment of the tube, m
Re	Reynolds number
Sb	density of the ball, kg/m^3
Sf	density of the fluid, kg/m^3
T	time interval of the falling ball, s
$\bar{U}$	average axial velocity, m/s
v_r	radial velocity, m/s
v_z	axial velocity, m/s
y	modified radial distance, m^2
z	axial distance, m

Greek Letters

α	constant in Equation (2.1)
β	constant in Equation (2.1)
γ	depth of the cavity, m
δ	width of the ridge, m
Δ	difference
ϵ	width of the cavity, m
λ	index of refraction
u	dynamic viscosity, mPa.s
ρ	mass density of the fluid, kg/m^3
υ	kinematic viscosity, m^2/s
Ψ	stream function
ω	vorticity
ζ	(radial distance)(vorticity)

Superscripts

*	dimensional quantity
_	average

Subscripts

i	axial index
j	radial index
w	wall

1. INTRODUCTION

Many problems in nature and in engineering involve the flow of fluids at low Reynolds numbers. The particular problem of interest in this study involves flow through internally corrugated tubes as occurs in living plants, mammalian circulation systems, narrow capillary tubes and porous media. In such tubes, flow occurs through the central portion while pockets of fluid circulate within the cavities or depressions at the wall. That is the flow structure is divided in two domains or separated. Studies on creeping flow in cavities have been motivated by the fundamental interest in the phenomenon of separation flow at low Reynolds number. Separation and formation of vortices may lead to changes in drag on a body or pressure gradients for internal flows.

For example, abnormal flow conditions develop in mammalian circulatory systems due to boundary irregularities and the flow patterns can be an important factor in the development and progression of arterial diseases. The boundary irregularities in the blood vessels are caused by deposits of intravascular plaques on or the loss of compliances and formation of periodic constrictions by the vessel wall[Chow and Soda, 1972]. Such wall irregularities are normally detrimental to the effective performance of the circulatory system. In the other systems, flow separation and vortices appear beneficial. An example is in living plants.

Water absorbed by the roots of higher terrestrial plants is transported over long distances to the leaves via xylem vessels and tracheary elements[Jeje, 1985].

Xylem vessels are porous-walled, closed ended microcapillaries of various lengths organized into intricate network structures. In many plants, secondary cellulosic strands form rings at intervals or spirals inside the capillary channels. These appear to improve the capacity of xylem vessels to convect water at necessary rates towards the leaves at fixed driving potential or pressure gradients. That is, the irregularities aid in drag reduction.

The latter example, and the need to understand macro-scale flows at microscopically irregular walls of tubes, has motivated this study. The model consists of rings of two internal diameters arranged alternately. The rims of the rings are sharp and such that they form separation and attachment lines for the flow. It is of interest to determine how variations in ring structures affect the flow patterns and the pressure gradients along tubes of irregular geometry.

1.1 Objectives and Scope of Study

The study involves both experiments and numerical simulation. The flow occurs at Reynolds number (based on the diameter of the narrower rings) less than 2. Such flows are in the creeping range as anticipated for the ascent of sap in plants. The objectives are to establish which geometric arrangements lead to the lowest pressure drop per unit length of the tube and to correlate this to the flow patterns developed. The controlling parameters are the aspect ratios of the recesses and the mean flow rates through the ducts. The geometry is axisymmetric.

Experiments involve the flow of water-glycerine mixtures at high viscosity, pressure drop measurements and flow visualization using hydrogen bubbles.

Numerical simulation of the flow was performed by solving a finite-difference form of the complete Navier-Stokes equation. Because different length scales exist for the core flow and the cavities, the equations were solved separately for the two regions and both velocity and velocity gradients were matched in an overlaying region. The equations in cylindrical coordinates were solved by the interactive approach[Brandeis and Rom, 1981]. The interactive method involve solving the equations for the two regions sequentially whenever a cavity is encountered. Finally, the numerical results are compared with those of experimental.

1.2 Physical Description of Domain

A schematic diagram of the channel and expected flow structures is shown in Figure 1.1. The figure shows periodic cavity on the wall of the circular tube and fluid is flowing through the tube. Cavity ABCD is open and one or more vortices could be trapped within. Two or more attachment/separation points may exist in the cavity. For narrow cavities (short CD), A and B represent the two branch or stagnation points. If CD is wide, at least two other branch points may exist along that wall and more than one vortex will be trapped.

Over the ridge BE, a bubble of near stagnant fluid may also exist depending on the Reynolds number.

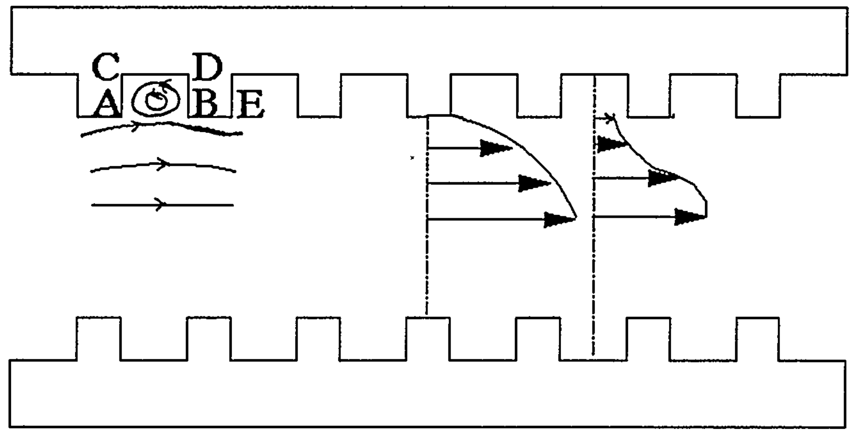

Fig. 1.1: Physical description of flow domain.

2. LITERATURE REVIEW

The fact that microscopic structures at a wall can effect drag reduction on an external surface or a decrease in pressure drop in pipe flows has been documented[Gaudet, 1987]. It is an issue of great curiosity and it has generated considerable commercial interest, particularly with regards to long distance transport of hydrocarbon fluids from production sites to markets[Weiss, 1993]. Primary attention has been given to the laminar sublayers of turbulent flows on surfaces with riblets. These are fine, stream-wise aligned surface grooves at pipe walls. Such structures have been indicated capable of reducing the overall drag or pressure drop by ~ 8%. For flows which are entirely laminar, Taylor[1971, Figure 4] has experimentally demonstrated, for rotating flows between two flat plates - one of which is grooved in circular patterns, that the frictional resistance can be lowered. In this geometry, the grooves are also stream-wise oriented.

The mechanisms for drag reduction for the turbulent and laminar flows are expected to be different. With turbulent flows in the external stream, riblets are suggested to align moving vortical streaks which are close to the bounding surface and bursts (or small jets) outside the laminar boundary layer. Thus wall shear patterns are controlled. For laminar flows, swirling eddies, like corkscrews trapped in the grooves, may be the agents for drag reduction in Taylor's experiments. Alternately, the recesses filled with fluid provides partial slip at the apparent boundaries defined by the plane of the ridges. Slip is reflected in a lower overall frictional resistance even with the considerable increase in fluid contact area.

When the grooves are oriented perpendicular to the direction of the stream, as is of current interest, two-dimensional ring vortices are trapped and maintained within the recesses. These may act as roller-bearings under certain conditions, to cause a reduction in frictional resistance to the flow situation.

In the following, the literature pertinent to the current study is briefly reviewed. Different structures for periodic surface irregularities (step, triangular, trochoidal and sinusoidal channels) have been considered by other investigators. Single deformations at the walls (projections and cavities with step and rounded contours) have also been examined. The focus is here on slow flows through periodic configurations, in particular with step changes.

2.1 Flow in Corrugated Tubes

The motivation for existing studies have been predominantly to model the micro-channel flows through granular porous media as have been idealized by Scheidegger[1957]. Such flows have low Reynolds number and the diameter of a pore expands and contracts alternately in the stream-wise direction. Both experimental and numerical simulation using equations of motion have been undertaken. Studies closest to the current one in terms of the geometry of the flow channels and the regime of flow were undertaken by Dullien and Azzam[1973, 1977] and Jeje[1985]. These will be reviewed first.

2.1.1 Channels with Step Changes

Dullien and Azzam[1973] presented experimental results on flow rates and pressure gradient measurements through corrugated tubes assembled from flat-surfaced discs (3.175 mm thick) with different diameter holes bored through them. The test section was ~ 0.18 m long and the diameter of the four-size holes ranged from 0.43 to 4.6 mm. Different combinations, in pairs, of two bore sizes were used to construct fifteen different corrugated tubes, the axial cross-sections of which form square waves with sharp edges. In such an arrangement, the stream-wise length of an internal recess equalled the length of the ridge, unlike the configurations in the present study. The flow stabilization arrangements up- and down-stream of the test sections were not mentioned although they indicated that end effects were checked for and found negligible through varying the length of the test section. The Reynolds number for the flow (apparently of water) ranged from 2 to 700. The plot of a typical run showed that the fluid flow rate was linearly related to the pressure drop across the test section at low pressures but the flow rate was slower than this linear pattern at an overall pressure gradient in excess of ~ 1 Pa/m. That is the flow resistance had increased relative to the flow rate. This is reflective of the non-Darcian effects associated with inertia in porous media [Scheidegger, 1957].

Through volume-averaging the Navier-Stokes equation, Dullien and Azzam[1973] were able to derive a form of equation similar to the empirical Forchheimer modification to Darcy's law. This equation

$$\nabla\langle p\rangle = \alpha\mu v + \beta\rho v^2 \tag{2.1}$$

has two parameters (α, β) which are constants in Forchheimer's equation but dependent on the flow field in the author's expression. The second term on the right is the correction introduced to account for inertial effects in non-Darcian flow. The author's effort were directed to obtaining values for α and β as related to the flow geometry.

Dullien and Azzam[1973] also discussed the issue of the area of voids at a cross-section of a porous media which is useful for calculating pore velocities characteristic for the flow. The volume-averaged quantity which corresponds to the Dupuis-Forchheimer application and the cross-section of the narrower of the pore diameters were identified as possible choices. This issue is also important in the application of a characteristic diameter for scaling of the flow through pores of different diameters in series. When the recesses are span-wise narrow but radially deep, i.e. the diameter of the larger pore is much greater than that of the narrow one, the volume-averaged area (which is volume of a repeating unit divided by its length) and consequently an equivalent diameter calculated from it has no physical significance. The diameter of stream tube for the flow, although varying periodically downstream, may not be significantly different from that of the narrower tube. On the other hand, if the axial length of the recessed region is significant and the indentation is shallow, i.e. the diameter of the bigger pore is only slightly bigger than the narrow one, the diameter of the stream tube may vary between the extremes. Under such circumstances, branch points (attachment and separation) may exist at the recessed wall and the geometry approximates a series of orifice plates at wellspaced intervals in a channel. An equivalent diameter based on volume-averaging may then be useful but its value would be nearly the same as for the narrow pore. From these arguments and for consistency of presenting the results, the diameter of the narrow tube is chosen as the characteristic length scale for the current work.

The same authors, Azzam and Dullien[1977], undertook a numerical simulation of flow through the same tubes as in the foregoing study. They solved the complete Navier-Stokes equation for steady flow for one cycle of the periodic structure. They elected to use the axial length of the cycle (or wavelength) as the characteristic dimension instead of a diameter. Implicit in their interpretation is that geometric similarity for the tubes implies dynamic similarity for the flow patterns since values for the ratio of the diameter of the narrow pore to the wavelength was considered to be the parameter which determined the existence of circulation within the recesses irrespective of the absolute values for width and depth of the recesses. Experimental observations, such as reported in this study, does not support such a conclusion or inference. The problem formulation suffered from two difficulties. One is that vorticity had to be prescribed at the wall of the channel without reference to the singularities (and source of concentrated vorticity generation) near the sharp corners of the square contours. The second difficulty is that the inlet to the cycle of interest was assumed to have a parabolic flow profile as the initial form in an iterative procedure involving corrections through the use of the solution for downstream edge (i.e. the start of another structure cycle). Results from such a technique are sensitive to the selected inlet profiles, particularly from a branch point.

The plots in their figure 4 suggest that flow profiles are essentially parabolic over a major fraction of the length of a ridge. This thereby excludes the formation of a bubble of near stagnant fluid over the projections which are the inner surfaces of the narrower tube. A more rigorous approach, as adopted here requires that an inlet region of constant diameter and adequate length be included such that the boundary condition (at the inlet) is known unequivocally. Calculations also should be done to include a number of cycles in recognition that, though the flow will be locally steady, flow development occurs downstream.

The results on pressure drop were also not as informative as required. The parameter p^+ (termed normalized pressure) will not be unity at the inlet to the tube as indicated. It may be less than or equal to zero. Plots of this variable versus distance (Figures 7 and 8) provides no information with regards to the relative values of the pressure gradients for the different tubes. Finally, the authors compared the pressure drops calculated to that evaluated using Hagen-Poiseuille's equation. For the latter, velocity profiles have to be assumed fully developed over each of the segment of constant bore. They used this ratio to define an "excess momentum loss factor". Such a comparison may be assumed irrelevant for structures with short segment lengths. A comparison with results for a constant diameter tube at similar Reynolds number may be more appropriate.

The only other study known to the author of this study with step changes in the channel diameter is that of Jeje[1985]. In this experimental study, pressure gradients were measured along corrugated tubes of three types. It was demonstrated that, at low Reynolds number, (<1), resistance to flow decreased for the irregular walled tubes compared to smooth walled channels. Trapped laminar vortices are suggested to aid in drag reduction and the flow patterns were found irreversible even at Reynolds number as low as 0.08. It is this study which has been expanded on in this investigation.

2.1.2 Flow in Periodic Cavity

Payatakes et al.[1973] numerically solved the steady-state Navier-Stokes equations for an incompressible Newtonian fluid through a periodically constricted tube. They retained all the terms of the Navier-Stokes equations including the nonlinear inertia terms. The authors simulated the geometry which is connected with the modelling of a packed bed of sand. The authors calculated the streamlines, axial and radial velocity profiles, pressure profiles and the dimensionless pressure drop versus Reynolds number relation. Their Reynolds number varied from 1 to 75. Payatakes et al.[1973] based their Reynolds number on volumetric (volume-averaged) diameter for one cycle of the periodic structure. The volumetric diameter was defined as the diameter of a cylindrical smooth tube which has the same volume and length as the periodic constricted tube. Their plots of friction factor versus Reynolds number at different volumetric diameter (Figure 9) shows that with an increase in volumetric diameter, friction factor decreases, not increases as concluded by Batra[1969] and Dullien and Batra[1970]. Payatakes et al.[1973] suggest that the results should be correlated not only with volumetric diameter alone, as was done by

Batra[1969], but with volumetric diameter and amplitude of the constricted tube. They pointed out that even for fixed values of volumetric diameter and amplitude, the friction factor of a periodically constricted tube is not uniquely determined but that it also depends on the geometry of the wall.

Batra et al.[1970] experimentally investigated the effect of geometric parameters for laminar flow through irregular surfaced rectangular tubes. The nominal diameters of the narrower segment were 6.35 mm and 9.53 mm. The periodically convergent-divergent wall structures were triangular in profile. The authors determined friction factor values for the Reynolds number range of 1 to 2000. Volume-averaged mean diameter was used to calculate Reynolds number and friction factor. They observed that for wavy tubes, the measured friction factors deviate markedly from those for smooth tubes. For uniform channels (amplitude-to-wavelength ratios ranging between 0.0090 and 0.0169) Fanning friction factors follow the relationship $f=18/Re$. For wavy channels (depth-to-mean width ratios ranging from 0.0112 to 0.0550) there was no effect on the frictional pressure drops due to the waviness of the narrow side walls. For wavy channels having larger values of depth-to-mean width ratios (0.0742 to 0.1855) the friction factor values are higher compared with those of the uniform channel.

Steady axisymmetric behaviour of a fluid flowing in the laminar regime through a corrugated tube was studied by Savvides and Gerrard[1984]. They solved the vorticity and stream function transport equations for an incompressible fluid flowing through a tube containing triangular grooves perpendicular to the flow direction by a finite difference technique.

The geometrical parameters and Reynolds number were varied to examine variations in the patterns of flow separation. The geometric parameters were width-to-diameter and depth-to-diameter ratios for the cavities.

The authors calculated the product of Reynolds number and dimensionless pressure drop along a corrugation cycle. In a corrugated tube at low Re-values, Re($-\Delta P/\Delta z$) was found to be independent of Re but the parameter was higher than 32, the value for a smooth straight tube. The diameter D in their calculations was the maximum value in the channel, not one defined by a stream tube or the narrower segments of the channel. Thus both Re and $\Delta P/\Delta z$ might have been overestimated. They varied their Reynolds number from 10 to 200.

2.1.3 Single Cavity

Bozeman and Dalton[1973] numerically solved the Navier-Stokes equations for the steady two-dimensional flow of a viscous incompressible fluid in a single closed rectangular cavity. The main objective of the authors was to perform a systematic evaluation of four different methods of finite difference equations. The Reynolds number range was from 10 to 1000. It is not clear from their work how they calculated the Reynolds number. They obtained asymmetric flow patterns in cavities of aspect ratios (depth/width) ranging from 1 to 2.

Pan and Acrivos[1967] observed the flow patterns in a single closed rectangular cavity where the motion was induced by the uniform translation of the top wall. The authors studied the flow patterns for Reynolds number ranging from 20 to 4000. They based their Reynolds number on the width of the cavity and velocity of translation of plate. They authors concluded that, for deep cavities, the viscous and inertia forces should remain of comparable magnitude within the whole domain. On the other hand, for shallow cavities, the steady flow should consists essentially of a single core of streamlines with viscous effects being confined to thin shear layers near the boundaries.

Shen and Floryan[1985] studied low Reynolds number flows over single closed rectangular cavities. The numerical results were obtained the Reynolds number value of 0.01. They based their Reynolds number on the depth of the cavity. The authors calculated the streamlines inside the cavity in details for various aspect ratios (0.5 ~ 4.0). They repeated their calculations with the null Reynolds number and found that the flow patterns to be exactly the same as for Re=0.01, and the values of the stream function were negligibly different. They considered pure Couette[Schlicting, 1979; p. 6] and pure Poiseuille[Schlicting, 1979; p.11] flow and concluded that the flow patterns were slightly or not affected while the values of the stream function were quite different.

Friedman[1970] studied the flow of a homogeneous viscous fluid in a straight circular pipe containing a single recess. He solved the complete Navier-Stokes equations for Reynolds number ranging from 0 to 500. The author based his Reynolds number on the radius of narrower segment of pipe and initial velocity. He assumed flat velocity profile at the inlet to the pipe and the parabolic profile far downstream. He presented the development of the velocity along the axis. In the case of a flow in a straight circular pipe, the velocity along the axis is an increasing monotonic function of z (pipe axis). If a recess is added to the pipe, the development of velocity along pipe axis is quite different. For small Re, it grows first from 1 to a local maximum, then it drops to a local minimum, and at last turns back into an increasing monotonic function, and tends asymptotically to 2. This is to be expected since the main separating streamline "widens" the pipe and therefore reduces the velocity field. This phenomena depends mainly of Re and the width of the recess. It is stronger for small Re and cavity width $>>$ 1.

Sinha et al.[1982] used smoke visualization, static pressure measurements, and hot wire anemometry to investigate flow in a cavity driven by a laminar boundary layer. Reynolds numbers, based on the cavity depth, were 662, 1324 and 2648. The authors classified the cavities as shallow-closed, shallow-open, open and deep based on depth/width ratio of the cavities. They found that the pressure distribution was characterized by negative pressure over most of the cavity floor followed by a small pressure recovery in the downstream face of the cavity.

Mehta and Lavan[1969] solved numerically the problem involving flow in a single closed rectangular cavity, located in the lower wall of a two-dimensional channel. To minimize the number of parameters, the authors assumed the channel length to be infinite and the upper wall of the channel was moved with a constant velocity. They calculated streamline patterns inside the cavity for aspect ratios (depth/width) of 0.5, 1.0 and 2.0 and for Reynolds numbers of 1, 10 and 100.

Reynolds number was based on the width of the cavity. The authors concluded that the position of the separating streamline was affected by the numerical treatment of the singularity in the vorticity field at the external corners.

Higdon[1985] studied shear flow over ridges and cavities in low Reynolds number range. He solved the Navier-Stokes equations in two-dimensional domain. The author obtained streamline patterns, velocity profiles and shear-stress distribution along the walls in cylindrical and rectangular shaped ridges and cavities. He did not mention the basis of his calculating the Reynolds number as well as the values of Re at which he performed his calculations. He employed these results in a discussion of the effect of the flow pattern on convective transport processes.

2.1.4 Interactive Methods

Brandeis and Rom[1980] proposed an interactive model for numerical computation of laminar separated flow. The authors divided the flow field into three regions, applying a simplified mathematical model in each of them; (a) outer flow for which the full potential equation (hyperbolic) was used; (b) viscous, laminar sublayer in which the compressible boundary-layer model (parabolic) is used; (c) recirculating flow modeled by the incompressible Navier-Stokes equations (elliptic). The method employs matching of flow variables along the overlapping boundaries of the regions. The interactive method in general require significantly smaller computer time as well as memory space, making their use economically preferable. They based their Reynolds number on the width of the cavity for cavity Reynolds number and distance from the leading edge of the plate to the beginning of the interaction for the outer two zones Reynolds number. The authors obtain streamline patterns, vorticity contour map for a cavity of aspect ratio 2 at Reynolds number of 5.4 based on the cavity width. The flow patterns were asymmetric about the midplane of the cavity.

Brandeis and Rom[1981] modified their three-layer interactive method two-layer model for computation of viscous flow in a cavity with recirculation for cavity of aspect ratio (depth/width) of 1 at Reynolds number based on cavity width of 5.4. The "matching model" matches the velocities and their gradients at the interface of the two computation domain.

Present work uses this two-layer interactive method in numerical simulation. The overlapping region was taken to be one grid size wide in the direction perpendicular to the flow.

2.1.5 Flow in a Convergent-Divergent Tubes

Christiansen et al.[1972] numerically solved the general equations of motion for laminar flow of Newtonian fluids from a larger tube of circular cross-section through an abrupt contraction into a coaxial tube of smaller diameter. They varied the ratio of the diameter of large tube to that of the smaller tube from one to eight and studied the radial and axial velocity profiles. The authors varied the Reynolds number from 0.01 to 500, which was based on the diameter of the smaller tube. They calculated the dependence of axial velocities on Reynolds number and found that with the increase of Reynolds number the parabolic profile becomes flat at the tube axis.

Cheng[1972] obtained numerical solutions of the Navier-Stokes equation for viscous, incompressible fluid flow in an arbitrary internal passage. The author used finite element method to overcome the difficulties arising from the nonlinearity of the governing equations and the complexity of the boundary conditions. Cheng[1972] calculated the shear stress in the domain of computation at Reynolds number ranging from 0 to 100, and the contraction parameter (width of narrow channel-to-width of the bigger channel) ranging from 0.2 to 0.6. Reynolds number was based on half-channel width. He observed a sharp increase in shear stress near the minimum cross-section and the maximum shear stress occurs slightly upstream of the narrowest cross-section.

3. ANALYSIS AND NUMERICAL MODELLING

The flow fields for the present study are described by the Navier-Stokes and continuity equations. The coordinate system is cylindrical and axisymmetric. Swirling motions are absent. Therefore, at steady-state, only the space variables r^* and z^* constitute the independent variables for the system. The Navier-Stokes equations in the primitive variables (v_r^* and v_z^*) is formulated in terms of stream function and vorticity transport equations. The resulting expressions are discretized using a finite difference technique and solved numerically. The method is described in this chapter in detail.

3.1 Flow Fields

The flow domain may be divided into two zones. Flow through the core or central portion of the tube, zone I in Figure 3.1, is driven by pressure forces and governed by viscous and inertia forces. Within the cavity, zone II, the flow is driven by the shear forces at the boundary with zone I. Velocities are lower in the cavity and viscous forces assume higher significance.

3.2 Primitive Equations

The constitutive equations for both zones are the continuity equation

$$\frac{1}{r^*}\frac{\partial}{\partial r^*}(\rho r^* v_r^*) + \frac{\partial}{\partial z^*}(\rho v_z^*) = 0 \qquad (3.1)$$

and the equations of motion given in the r^*-direction by

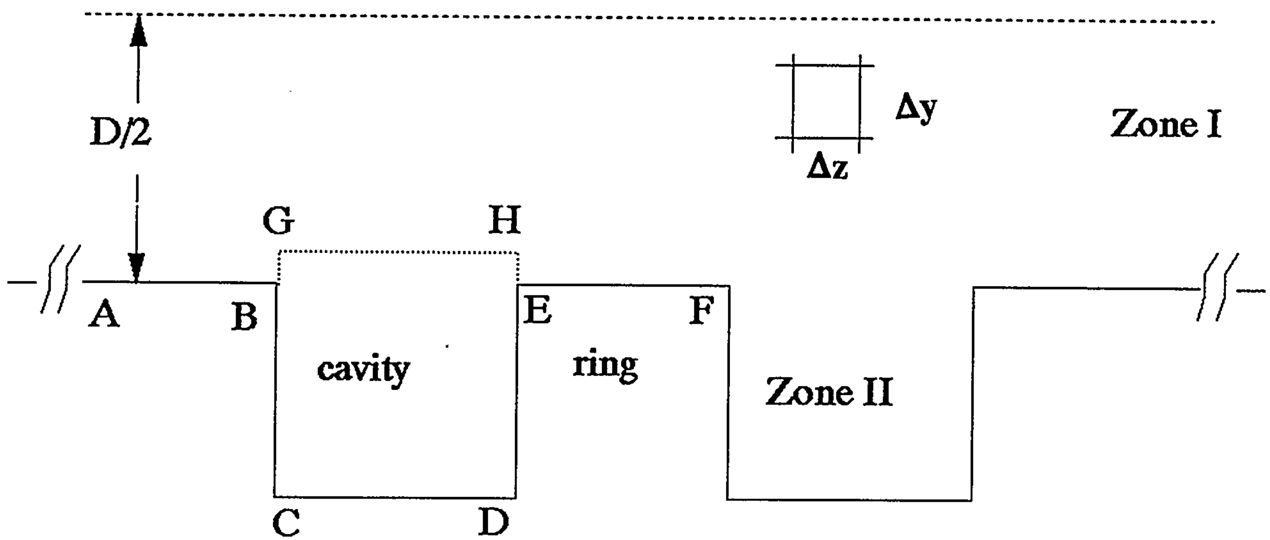

Figure 3.1: Schematic Diagram of Computational Domain

$$v_r^* \frac{\partial v_r^*}{\partial r^*} + v_z^* \frac{\partial v_r^*}{\partial z^*} = -\frac{1}{\rho}\frac{\partial P^*}{\partial r^*} + \nu\left[\frac{\partial}{\partial r^*}\left(\frac{1}{r^*}\frac{\partial}{\partial r^*}(r^* v_r^*)\right) + \frac{\partial^2 v_r^*}{\partial z^{*2}}\right] \quad (3.2)$$

and in the z^*-direction by

$$v_r^* \frac{\partial v_z^*}{\partial r^*} + v_z^* \frac{\partial v_z^*}{\partial z^*} = -\frac{1}{\rho}\frac{\partial P^*}{\partial z^*} + \nu\left[\frac{1}{r^*}\frac{\partial}{\partial r^*}\left(r^* \frac{\partial v_z^*}{\partial r^*}\right) + \frac{\partial^2 v_z^*}{\partial z^{*2}}\right] \quad (3.3)$$

It is assumed for these equations that the fluid is Newtonian (μ is constant), incompressible and there are no body forces. The tube is symmetric, so only axial and radial velocities were considered. These equations are written in the primitive variables of velocity components, v_r^* and v_z^*, and pressure P^*, and the fluid properties of mass density ρ, and kinematic viscosity, υ.

All the variables in equations (3.1) to (3.3) are dimensional. Pressure can be eliminated from equations (3.2) and (3.3) by cross-differentiating and subtracting the resulting expressions[Schlichting, 1979].

3.2.1 Core Region

Zone I is the core region through which the fluid is in axial translation. This region includes entrance and exit lengths of a straight tube which has the same diameter as the narrower pore of the corrugated tube and ten cycles of the periodic step changes in channel diameter. The entrance length was chosen as equal to two (2) times the narrower segment of the tube. The initial set of step changes constitute the flow development domain. It is assumed that the flow is fully developed before reaching the inlet and any upstream diffusion of vorticity[Vrentas et al., 1966] is confined to the entrance region. Through adopting the following dimensionless variables, with a characteristic length chosen as the diameter D of the narrower tube and the average velocity $\bar{U}$ through such tube as the nondimensionlizing factor for the velocity[Salim, 1994]:

$$
\begin{gathered}
r = \frac{r^*}{D}, \quad z = \frac{z^*}{D} \\
v_r = \frac{v_r^*}{\bar{U}}, \quad v_z = \frac{v_z^*}{\bar{U}} \\
P = \frac{P^*}{\rho \bar{U}^2}, \quad Re = \frac{\rho \bar{U} D}{\mu}
\end{gathered} \tag{3.4}
$$

and also defining stream function (Ψ) and vorticity (ω) such that:

$$
\begin{gathered}
v_r = \frac{1}{r}\frac{\partial \Psi}{\partial z}, \quad v_z = -\frac{1}{r}\frac{\partial \Psi}{\partial r} \\
\zeta = r\frac{\partial v_r}{\partial z} - r\frac{\partial v_z}{\partial r}, \quad \omega = \frac{\zeta}{r}
\end{gathered} \tag{3.5}
$$

Equations (3.1) to (3.3) can be transformed into the nondimensional vorticity transport and stream function equations,

$$
\frac{\partial}{\partial r}(\zeta v_r) + \frac{\partial}{\partial z}(\zeta v_z) - \frac{v_r \zeta}{r} = \frac{1}{Re}\left[\frac{1}{r}\frac{\partial}{\partial r}\left(\frac{1}{r}\frac{\partial \zeta}{\partial r}\right) + \frac{\partial^2 \zeta}{\partial z^2}\right] \tag{3.6}
$$

and

$$
\zeta = \frac{\partial^2 \Psi}{\partial z^2} + r\frac{\partial}{\partial r}\left[\frac{1}{r}\frac{\partial \Psi}{\partial r}\right] \tag{3.7}
$$

The coordinates are further transformed, by defining

$$y = r^2 \tag{3.8}$$

so that for equal increments in y, the increments in r are smaller near the walls than near the axis of the tube. The rationale for this transformation is that the mesh points are concentrated near the wall where the vorticity gradients are largest[Ralph, 1986]. Equations (3.6) and (3.7) then become:

$$\zeta = \frac{\partial^2 \Psi}{\partial z^2} + 4y\frac{\partial^2 \Psi}{\partial y^2} \tag{3.9}$$

$$2\sqrt{y}\frac{\partial}{\partial y}(\zeta v_r) - \frac{v_r \zeta}{\sqrt{y}} + \frac{\partial}{\partial z}(\zeta v_z) = \frac{1}{Re}\left[4y\frac{\partial^2 \zeta}{\partial y^2} + \frac{\partial^2 \zeta}{\partial z^2}\right] \tag{3.10}$$

and vorticity

$$\omega = \frac{\zeta}{\sqrt{y}} \tag{3.11}$$

where

$$v_r = \frac{1}{\sqrt{y}}\frac{\partial \Psi}{\partial z}, \quad v_z = -2\frac{\partial \Psi}{\partial y} \tag{3.12}$$

3.2.2 Boundary Conditions

Solutions to the elliptic equations require the specifications of the boundary conditions. A parabolic velocity profile is prescribed at the entrance to the flow arrangement.

At $z = 0$ for all y

$$\zeta = 16y, \ \Psi = 0.125(1-4y)^2 \tag{3.13}$$

$$v_z = 2(1-4y), \ v_r = 0 \tag{3.14}$$

Along the centre line, i.e., y = 0 for all z

$$\zeta = 0, \ \Psi = 0.125, \ v_r = 0 \tag{3.15}$$

At the outlet of the long exit tube (~ 5D), the boundary conditions are,

z = L/D for all y

$$\zeta = 16y, \ \Psi = 0.125(1-4y)^2 \tag{3.16}$$

$$v_z = 2(1-4y), \ v_r = 0 \tag{3.17}$$

At the walls, AB and EF, r=0.5 (Figure 3.1),

$$\Psi_w = 0, \ \left[\frac{\partial \Psi}{\partial z}\right]_w = \left[\frac{\partial \Psi}{\partial y}\right]_w = 0 \tag{3.18}$$

$$\zeta_w = 4y_w\left[\frac{\partial^2 \Psi}{\partial y^2}\right]_w \tag{3.19}$$

except at the branch points where ζ_w=0

Velocities and their gradients on line BE are matched with the solution of cavity region.

Axial pressure gradient was found from the equation of motion in axial direction from:

$$Re\left(-\frac{\partial P}{\partial z}\right) = 8\frac{\partial^2 \Psi}{\partial y^2} - 4y\frac{\partial^2 v_z}{\partial y^2} - \frac{\partial^2 v_z}{\partial z^2} + Re\left[2v_r\sqrt{y}\frac{\partial v_z}{\partial y} + v_z\frac{\partial v_z}{\partial z}\right] \qquad (3.20)$$

3.3 Cavity Region

In the cavity CDHG (as shown in Figure 3.1), the velocities are lower than in the core flow. Scaling of the equations for this region was done using the characteristics length γ, the depth of the cavity and the kinematic viscosity, υ; that is, υ/γ. Introducing the following dimensionless variables,

$$r = \frac{r^*}{\gamma},\ z = \frac{z^*}{\gamma},\ v_r = \frac{v_r^*}{\nu/\gamma}$$
$$v_z = \frac{v_z^*}{\nu/\gamma},\ P = \frac{P^*}{\rho(\nu/\gamma)^2} \qquad (3.21)$$

and also defining stream function (Ψ) and vorticity (ω) as follows:

$$v_r = \frac{1}{r}\frac{\partial \Psi}{\partial z},\ v_z = -\frac{1}{r}\frac{\partial \Psi}{\partial r} \qquad (3.22)$$

and

$$\zeta = r\frac{\partial v_r}{\partial z} - r\frac{\partial v_z}{\partial r},\ \omega = \frac{\zeta}{r} \qquad (3.23)$$

the resulting nondimensional vorticity transport and stream function equations are,

$$\frac{\partial}{\partial r}(\zeta v_r) + \frac{\partial}{\partial z}(\zeta v_z) - \frac{v_r\zeta}{r} = \frac{1}{r}\frac{\partial}{\partial r}\left(\frac{1}{r}\frac{\partial\zeta}{\partial r}\right) + \frac{\partial^2\zeta}{\partial z^2} \qquad (3.24)$$

and

$$\zeta = \frac{\partial^2\Psi}{\partial z^2} + r\frac{\partial}{\partial r}\left[\frac{1}{r}\frac{\partial\Psi}{\partial r}\right] \qquad (3.25)$$

The coordinates are transformed as was done for the core flow, using equation (3.8). The resulting equations are,

$$\frac{\partial^2\Psi}{\partial z^2} + 4y\frac{\partial^2\Psi}{\partial y^2} = \zeta \qquad (3.26)$$

and

$$2\sqrt{y}\frac{\partial v_r\zeta}{\partial y} - \frac{v_r\zeta}{\sqrt{y}} + \frac{\partial v_z\zeta}{\partial z} = 4y\frac{\partial^2\zeta}{\partial y^2} + \frac{\partial^2\zeta}{\partial z^2} \qquad (3.27)$$

where

$$v_r = \frac{1}{\sqrt{y}}\frac{\partial\Psi}{\partial z},\ v_z = -2\frac{\partial\Psi}{\partial y} \qquad (3.28)$$

3.3.1 Boundary Conditions

Boundary conditions which apply in the cavity are written below. The boundary GH is taken at one grid point inside in the inner region (Figure 3.1).

At the wall (lines BC, CD, DE),

Along the wall CD which is parallel to the tube axis,

$$\Psi_w = 0,\ \left(\frac{\partial\Psi}{\partial y}\right)_w = \left(\frac{\partial\Psi}{\partial z}\right)_w = 0 \qquad (3.29)$$

$$\zeta_w = 4y_w\left(\frac{\partial^2\Psi}{\partial y^2}\right)_w \qquad (3.30)$$

On the walls BC & DE which are perpendicular to the flow direction,

$$\zeta_w = \left(\frac{\partial^2\Psi}{\partial z^2}\right)_w \qquad (3.31)$$

Vorticity at the branch points and corners B, C, D and E vanishes[Roach, 1976]. Values for vorticity and stream function on line GH are obtained from the solution to the core zone equations.

3.4 Numerical Analysis

The system of partial differential equations which describes the flow fields is solved by a finite difference technique. Figure 3.2 shows the schematic of the computational domain used for the numerical analysis. A rectangular grid is laid on this domain. The mesh sizes are different in z and y directions. In order to predict the small scale flow pattern, a very dense grid structure is used. All the variables are defined at the mesh points where the horizontal and vertical grids intersect each other. Subscripts i and j refer to z and y coordinates respectively. The mesh spacings along the z and y directions are 'Δz' and 'Δy' respectively. Due to the limited storage capacity of the computing system and large CPU time required for the solution, the

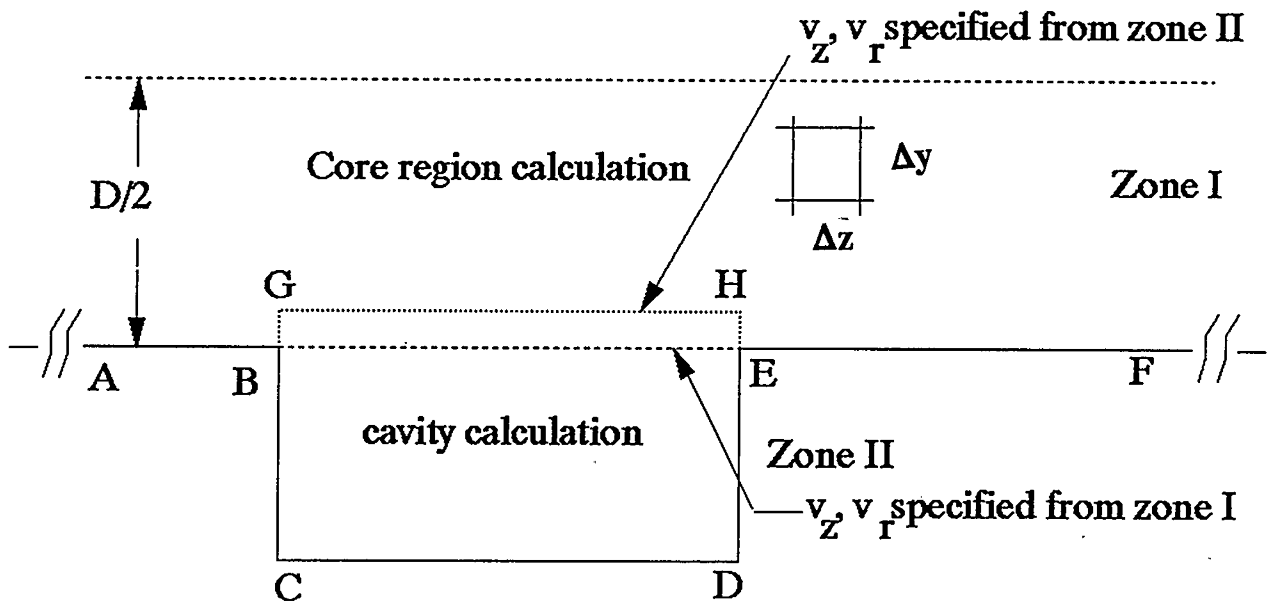

Figure 3.2: Schematic of the Overlapping Regions

used for Matching

computational domain was confined to 10 cavity lengths along the axial direction.

3.4.1 Discretization

The set of equation to be solved comprised of (3.6) and (3.7) for core region and (3.32) and (3.33) for cavity region. Since, the accuracy of central-difference is second order, all the derivatives were approximated by central differences. The finite difference forms of the equations (3.2) and (3.3) are obtained for core region as follows:

$$\sqrt{(j-1)\Delta y}\left[\frac{(v_r\zeta)_{i,j+1}-(v_r\zeta)_{i,j-1}}{\Delta y}\right]-\frac{(v_r\zeta)_{i,j}}{\sqrt{(j-1)\Delta y}}+\left[\frac{(v_z\zeta)_{i+1,j}-(v_z\zeta)_{i-1,j}}{2\Delta z}\right]$$
$$=\frac{1}{Re}\left[4(j-1)\Delta y\frac{\zeta_{i,j+1}-2\zeta_{i,j}+\zeta_{i,j-1}}{(\Delta y)^2}+\frac{\zeta_{i+1,j}-2\zeta_{i,j}+\zeta_{i-1,j}}{(\Delta z)^2}\right] \tag{3.32}$$

and

$$\zeta_{i,j}=\frac{\Psi_{i+1,j}-2\Psi_{i,j}+\Psi_{i-1,j}}{(\Delta z)^2}+4(j-1)\frac{\Psi_{i,j+1}-2\Psi_{i,j}+\Psi_{i,j-1}}{\Delta y} \tag{3.33}$$

For cavity region, the discretized equations are

$$\sqrt{(j-1)\Delta y}\left[\frac{(v_r\zeta)_{i,j+1}-(v_r\zeta)_{i,j-1}}{\Delta y}\right]-\frac{(v_r\zeta)_{i,j}}{\sqrt{(j-1)\Delta y}}+\left[\frac{(v_z\zeta)_{i+1,j}-(v_z\zeta)_{.}}{2\Delta z}\right.$$
$$=4(j-1)\Delta y\frac{\zeta_{i,j+1}-2\zeta_{i,j}+\zeta_{i,j-1}}{(\Delta y)^2}+\frac{\zeta_{i+1,j}-2\zeta_{i,j}+\zeta_{i-1,j}}{(\Delta z)^2} \tag{3.34}$$

and

$$\zeta_{i,j} = \frac{\Psi_{i+1,j} - 2\Psi_{i,j} + \Psi_{i-1,j}}{(\Delta z)^2} + 4(j-1)\frac{\Psi_{i,j+1} - 2\Psi_{i,j} + \Psi_{i,j-1}}{\Delta y} \tag{3.35}$$

where the velocity equations for both regions are discretized as follows:

$$v_{r_{i,j}} = \frac{1}{(j-1)\Delta y}\frac{\Psi_{i+1,j} - \Psi_{i-1,j}}{2\Delta z} \tag{3.36}$$

and

$$v_{z_{i,j}} = -\frac{\Psi_{i,j+1} - \Psi_{i,j-1}}{\Delta y} \tag{3.37}$$

3.4.2 Initialization and Boundary Conditions

Initialization conditions is based on a parabolic velocity profile in the main stream.

For $0 \le y \le 0.25$

$$\zeta = 16y, \; \Psi = 0.125(1-4y)^2 \tag{3.38}$$

$$v_z = 2(1-4y), \; v_r = 0 \tag{3.39}$$

(a) Calculation are initialized by prescribing values for ζ and Ψ. The conditions were discretized as follows,

Core region:

$$\zeta_{i,j} = 16(j-1)\Delta y, \ \Psi_{i,j} = 0.125(1-4(j-1)\Delta y)^2 \quad (3.40)$$

$$v_{z_{i,j}} = 2(1-4(j-1)\Delta y), \ v_{r_{i,j}} = 0 \quad (3.41)$$

Cavity Region:

Initialization conditions based on zero velocities in the cavities were used.

$$\zeta = 0, \ \Psi = 0 \qquad \text{for all } y \quad (3.42)$$

$$\zeta_{i,j} = 0, \ \Psi_{i,j} = 0 \quad (3.43)$$

where y varies from GH to CD.

and

$$v_{z_{i,j}} = v_{r_{i,j}} = 0 \quad (3.44)$$

(b) Inflow and Centreline boundary: Since no mesh points exists outside the boundary, the method of "reflection" was used to eliminate the grid point outside the boundary by replacing it with the point just one grid inside the domain.

Core Region:

At z = 0

$$\zeta_{i,j} = 16(j-1)\Delta y \quad (3.45)$$

$$\Psi_{i,j} = 0.125(1-4(j-1)\Delta y)^2 \quad (3.46)$$

At y = 0, or at the centreline due to the symmetry of the configuration

$$v_{z_{i,j}} = 2(1-4(j-1)\Delta y) \qquad (3.47)$$

$$\zeta_{i,j} = 0, \ \Psi_{i,j} = 0.125 \qquad (3.48)$$

$$v_{z_{i,j}} = \frac{\Psi_{i,j+2} + 3\Psi_{i,j} - 4\Psi_{i,j+1}}{\Delta y}, \ v_{r_{i,j}} = 0 \qquad (3.49)$$

(c) Wall: At the walls the velocity and their gradients are always zero, due to the "no-slip" condition.

Core Region:

Along the walls AB and EF (see Figure 3.2),

$$\zeta_w = 8j_w \frac{\Psi_{w-1}}{\Delta y} \qquad (3.50)$$

except at the branch points.

Cavity Region:

In the cavity region, due to the "no-slip" condition at the wall BC, CD and DE (see figure 3.2), the velocity and stream function are zero.

Along wall CD, parallel to the tube axis,

$$\zeta_w = 8j_w \frac{\Psi_{w-1}}{\Delta y}, \ \zeta_w = 2\frac{\Psi_{w-1}}{\Delta y} \qquad (3.51)$$

and on walls BC and DE which are perpendicular to the flow direction, vorticity being zero at the corners.

3.5 Solution Procedure

As the domain was divided into two regions, the continuity of solution between the two regions was ensured by matching the flow variables at the interface. For this purpose, a matching model[Brandeis and Rom, 1981], making use of partial overlap between the two computational regions, was utilized. The basic procedure of the matching model is to transform the variables at the interface between the two regions. That is, the variables calculated from one zone are scaled appropriately using the ratio of the scaling parameters. The overlap, presented schematically in Figure 3.2, facilitates matching not only the two velocity components, but their gradients as well.

3.5.1 Algorithm

The solution algorithm using Gauss-Seidel Implicit method is as follows.

STEP 1: The initial and boundary conditions are calculated from equations (3.38), (3,39) (3.40), (3.41), (3.42), (3.43), (3.44), (3.45), (3.46), (3.47), (3.48), (3.49), (3.50) and (3.51) for the appropriate computational region

STEP 2: For Core Region, the ζ and Ψ are calculated from equations (3.32) and (3.33)

STEP 3: Improve the velocities using equations (3.36) and (3.37)

STEP 4: The velocities and their gradients at GH boundary from the Core region to Cavity region undergo compatibility transformation using appropriate scaling criteria.

STEP 5: Continue the same calculation as in step 2 for the Outer region using equations (3.34) and (3.35)

STEP 6: Update the velocities in the cavity region using the updated values of ζ and Ψ

STEP 7: Transform the velocities and their gradients at BE boundary following the same procedure as in step 4

STEP 8: If $|| \delta\zeta ||_{avg} \leq 10^{-7}$ and $|| \delta\Psi ||_{avg} \leq 10^{-8}$, stop the calculation. Otherwise go to step 2.

The geometries and dimensionless variables of the nine corrugated tubes are presented in Table 3.1.

Table 3.1: Computational Grid Arrangements

	Δz	Δy	Grids at Inlet	Grids at Outlet	Grids per Cavity	Grids per Ring
Set 1	0.004	0.0033	500 x 76	1000 x 76	30 x 148	30 x 76
Set 2	0.004	0.0033	500 x 76	1000 x 76	54 x 148	30 x 76
Set 3	0.004	0.0033	500 x 76	1000 x 76	62 x 109	30 x 76
Set 4	0.004	0.0033	500 x 76	1000 x 76	152 x 136	30 x 76
Set 5	0.004	0.0033	500 x 76	1000 x 76	36 x 190	30 x 76
Set 6	0.004	0.0033	500 x 76	1000 x 76	62 x 118	30 x 76
Set 7	0.004	0.0033	500 x 76	1000 x 76	30 x 232	30 x 76
Set 8	0.004	0.0033	500 x 76	1000 x 76	62 x 85	30 x 76
Set 9	0.004	0.0033	500 x 76	1000 x 76	727 x 148	30 x 76

4. EXPERIMENTS

4.1 Experimental Set-up

A schematic diagram of the experimental apparatus is shown in figure 4.1. The apparatus was designed to operate at atmospheric pressure and constant temperatures between 10°C and 30°C. For all the runs, the temperatures were 23.5 ± 0.5°C. Viscosities of the test fluid, because of its sensitivity to temperature and its hygroscopicity (moisture absorption from air), were measured frequently under conditions of the experiments.

The apparatus consists of a flow pump, a storage tank, a water bath, a flow straightener, the test section, a separation tank, hydrogen bubble generator and a Validyne model 103 pressure transducer with Validyne model CD 223 display system. The test section consists of plexiglass tubes in three sections (A, B, C in Figure 4.1) submerged in a glycerin-water bath. The latter was provided to maintain constant temperatures around the test section and to minimize parallax for flow visualization and recording of flow patterns on photographic film. Refractive indices for glycerine-water mixtures and plexiglass are given in Table 4.1.

The glycerin-water mixture flow loop starts from the storage tank and the liquid flows through the flow straightener, sections A, B and C, into a separation tank. From the separation tank the fluid is drawn by a peristaltic pump and discharged into the storage tank. In transit after the pump, liquid is conducted through a water bath such that the temperature remains near room temperature.

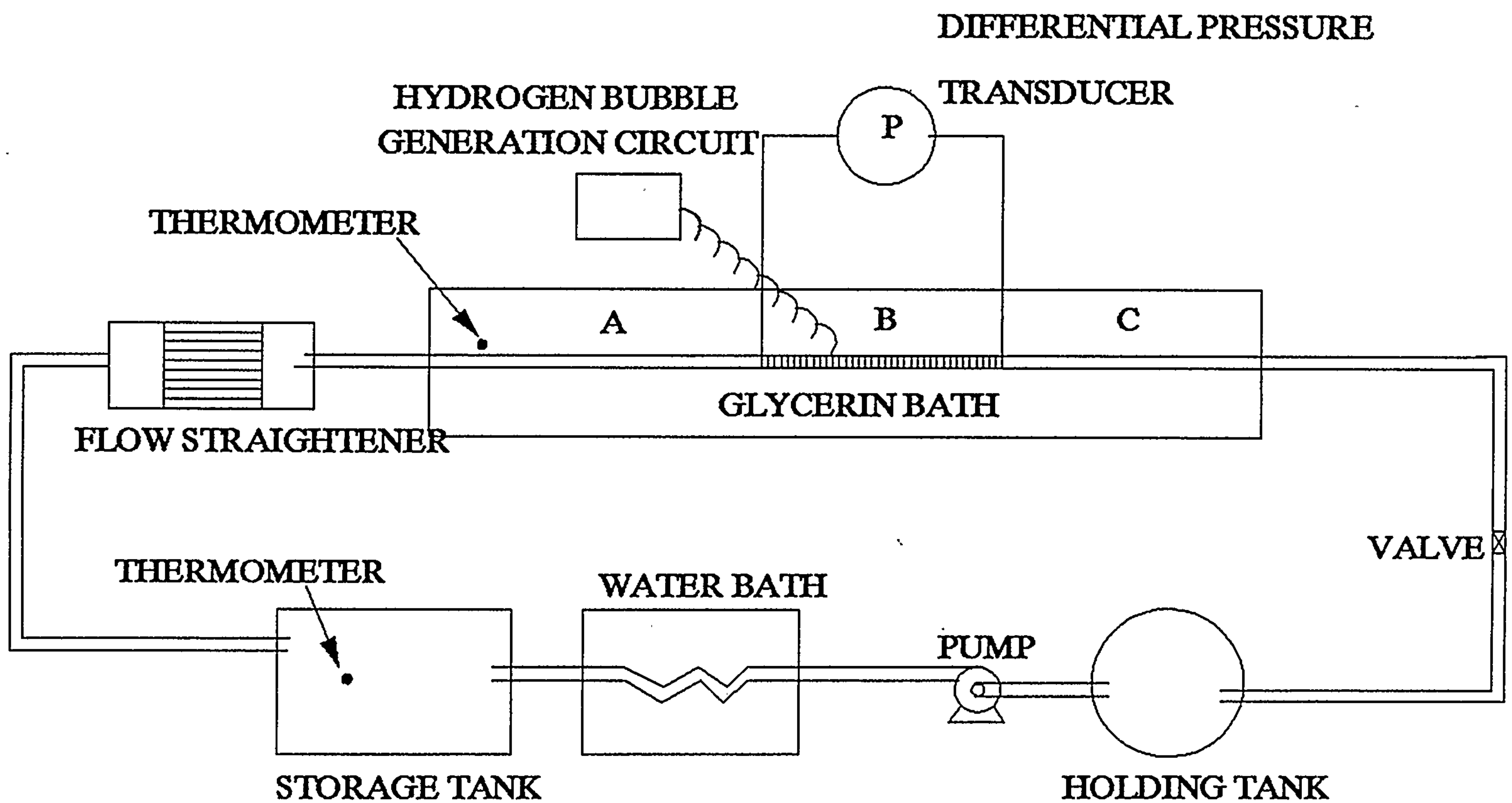

Figure 4.1: Schematic Diagram of the Experimental Setup

Pressure drop was measured across the central portion of the test section B using a calibrated Validyne DP 103-28 differential pressure transducer cell. The DP cell was connected to a Validyne CD 223 display device. Hydrogen bubble generators composed of thin platinum wires (dia. 0.045 mm) were used to mark the flow. One wire was located vertically through the tube axis several tube diameters into section A. This allowed determination of the centreline velocity for a fully developed parabolic profile in the straight, constant cross-section tube. Other wires were located after 5 to 10 cycles of the corrugated section. This allowed the monitoring of the flow patterns in the core and within the cavities downstream.

4.2 Flow Medium

In all experimental runs, the test or flowing medium was a mixture of glycerine and distilled water which initially contained 96 volume percent of glycerine doped with sodium sulphate. With time (~ weeks), the glycerine absorbed moisture from air and became diluted despite the location of a silica-gel column between the tank and the vent to the atmosphere. The viscosity, as measured, gradually decreased over the period of the experiments.

4.3 Fluid Properties

The flow through the corrugated tubes utilized the glycerine-water mixture. The physical properties of the water were taken from steam tables, and those of glycerine were determined experimentally.

Viscosities of glycerine-water mixtures were measured with the "Hoeppler Precision Vicosimeter". A spherical ball is allowed to fall through a known distance and the time of fall is measured by a stop watch. Using the time of fall and the densities of the ball and the fluid medium, the viscosity is calculated using Eq. 4.1 (see Table 4.1 for published values used for calibration). All the measurements were done at known temperature, ~ 23.5 ± 0.5°C and atmospheric pressure.

The viscosity in mPa.s or centipoises is given by the following formula:

$$\mu = T*(Sb - Sf)*B \tag{4.1}$$

wherein

u= absolute (dynamic) viscosity in centipoises

T= time interval of the falling ball, sec

Sb= density of the ball, gm/cc

Sf= density of the fluid at the measuring temperature, gm/cc

B= ball constant

Density of glycerine was measured using a pycnometer at room temperature and atmospheric pressure (see Table 4.1).

4.4 Preparation of the Test Fluid

A mixture of approximately 4% (by volume) water (doped with sodium sulphate) in glycerine was made as follows. A 1 ppm solution of the salt in water, was first made. Approximately 100 gm of sodium sulphate was dissolved in 950 ml of dist-

Table 4.1: Physical Properties of Glycerine-water mixture(20°C)*

% Glycerine in water	Density, ρ (kg/m^2)	Viscosity, μ (mPa.s)	Index of Refraction, λ
100	1261	1761.00	1.4735
96	1200	748.80	1.4674
92	1141	353.70	1.4613
84	1024	70.84	1.4462
80	966	47.88	1.4431
72	854	19.88	1.4310
60	691	6.40	1.4129
52	588	3.46	1.4011
Plexiglass			1.4900

*Ralph, 1986; CRC Handbook of Chemistry and Physics, 1982-1983, p. D-239.

illed water with continuous stirring. Then 1050 ml of the salt-water solution was added to 20 litres of glycerine in a tank. The solution was stirred for at least 30 min to ensure uniformity.

4.5 Procedure

At the beginning of each run, the flow line including the lines connected to the pressure transducer was cleaned of air bubbles. Bubbles were removed either by dismantling the system components or the use of a vacuum on the storage tank while re-circulation flow was maintained for ~ 4 hours. The bubbles then dissolved. After that, the liquid was allowed to flow by gravity from the elevated storage tank into the tube. This provided a nearly disturbance-free feed. The tank was vented to maintain pressure and isolated except for flexible inlet and outlet tubes so that vibrations were not transmitted from the pump. Silica gel, as noted above, was used in the vent line so that dilution of the hygroscopic glycerine-water mixture occurred only very slowly. The liquid passed through a flow straightener consisting of 11cm long by 0.455 cm diameter plastic straws in a 33.5 cm long by 8.5 cm diameter cylindrical tube. The mixture then flowed through a converging funnel before entering the inlet section of the test tube. The inlet section, denoted by A, is a tube of 1.97 cm diameter and 84 cm in length. The middle section, B, is the test section, where alternating rings of plexiglass having different inner diameters were assembled. The specifications of the rings used to assemble the test section are given in Table 4.2 and two and a half cycles of the corrugation are shown in Figure 4.2. The test section was about 60 cm

Table 4.2: Cavity and Ring Specifications

Type	Ring Spacing, cm δ	Cavity Width, cm ϵ	Cavity Depth, cm γ
1	0.239	0.238	0.392
2	0.239	0.428	0.389
3	0.239	0.488	0.198
4	0.239	1.194	0.341
5	0.239	0.287	0.574
6	0.239	0.488	0.239
7	0.239	0.238	0.748
8	0.239	0.488	0.050
9	0.239	5.730	0.390

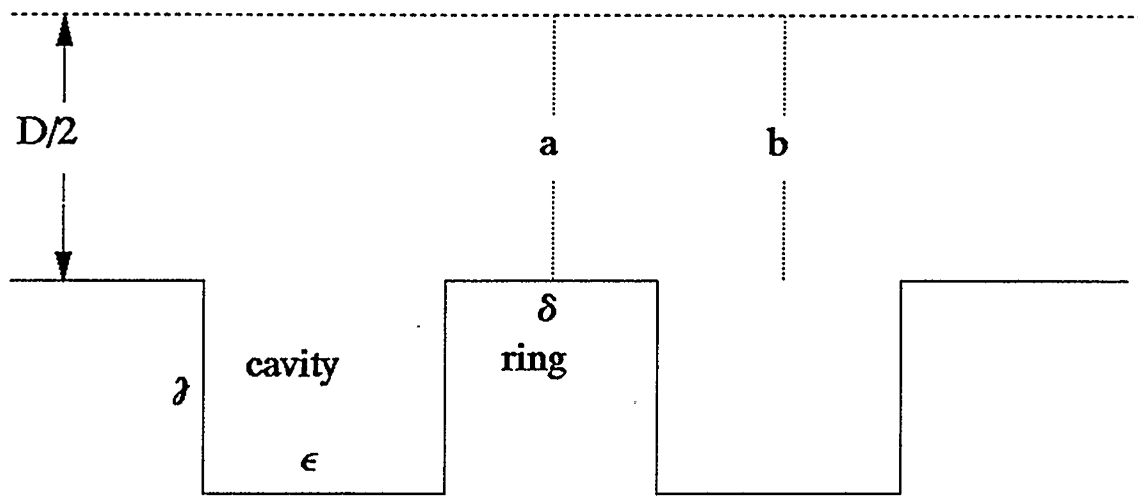

Figure 4.2: Schematics Diagram of Ring and Cavity

long. Thus between 10 and 126 cycles were in the test section which was connected to the exit section C. The latter was 60 cm long and 1.97 cm in diameter. Each run required approximately 1 hour to reach steady-state (as indicated by constant pressure drop and constant fluid level in the main storage tank) from a different setting of tank elevation. After reaching steady-state, if the flow was stopped and restored, fully developed flow was re-established in fractions of a second because of the high fluid viscosity[Bird et al., 1960, p.129]. After reaching steady-state, the pressure drop across the middle 40-50 cm of the test section and temperature of the glycerine bath were recorded. The centreline velocity in section A was determined by measuring the time interval required by the hydrogen bubbles to traverse a specified distance (10 cm.). The average velocity is half of this value. After the pressure drop and the flow rate were recorded, the set-up was adjusted for the next run. In this way, 8 to 10 flowrate settings were taken for one arrangement of rings. The same was repeated for other type of cavity specifications.

4.6 Flow-visualization experiments

Flow visualization experiments were confined to the cavity region in the middle of the test section. Flows in the core of the corrugated tube could also be monitored but these involve following individual bubbles located at different distances from the tube axis. Consecutive time-lines marked by the hydrogen bubbles and generated at known intervals may also be used to determine the velocity profiles at each cross-section of a cycle of the corrugated tube. These were not explored in this study. Of interest were the streamlines at the entrance to and within the cavities. These were marked by individual bubbles in prolonged exposures on photographic film. That is, streak photographs of illuminated bubbles were obtained of the pathlines.

The equipment consisted of a Nikon camera fitted with extension bellows and a 135 mm lens. This was on a heavy and stable mount to which a translating stage was attached. This arrangement allowed easy focusing and achievement of a 2-3 times magnification of the object located about 20 cm away. The test section was illuminated from the top from an angle of 30° to the vertical from the rear by two optics fibres attached to a light box. The light source was a tungsten-halogen bulb as used in projectors. The light was relatively cool at the ends of the fibres. At the back of the test section, a flat black card was placed at about 45° to the horizontal to provide contrast. This card was immersed in the bath of glycerine. The arrangement was similar to that used by Jeje[1985].

The procedures for taking pictures are as follows. The system was adjusted so that a steady flow occurred through the test section. This rate was measured. Then hydrogen bubbles, less than 0.2 mm but greater than 0.05 mm, were generated through adjustments of power and charge/discharge duties of the capacitors in the bubbles generator. The flow was then stopped. This allowed bubbles to rise under buoyancy into the cavity of interest. Between 15 and 30 minutes were required for 3-6 bubbles to travel about 2 mm into the cavity. Larger bubbles ascended too fast and thus will not define closed loops once flow is re-started and trapped vortices form. Bubbles that were too small dissolved before they reached the proper heights. When bubbles ~ 0.1 mm were in the cavity, the flow through the core was re-started. The bubbles then started to circulate with the stream to track the streamlines. Picture taking started after 1-2 minutes. Exposures were between 20 and 120 s, typically 30-60 s. For longer exposures, the bubbles (when large) may change trajectories due to buoyancy or (when small) shrink through dissolution of the gas to become invisible. It was essential to have the rings of the corrugated tube properly aligned to avoid swirling flows within the cavity which changed progressively the plane of re-circulation of the streamline. The circulation patterns could also be distorted if the projections or ridges made by the narrower bore discs were not in a horizontal line.

Pictures were taken under conditions similar to those for pressure measurements. Some of the results are presented in the following chapter and compared with results from numerical simulation.

5. RESULTS AND DISCUSSION

Experimental and calculated results for nine configuration of corrugated tubes are presented in this chapter. Velocity profiles calculated over one cycle of the corrugation are presented in Figures 5.1 to 5.9. Pressure gradients from experiments are plotted versus Reynolds number in Figures 5.10(a and b) and friction factor versus Reynolds number in Figures 5.11(a and b). The invariance of the product of friction factor and Reynolds number for all the flow configurations is demonstrated in Figure 5.12. Some calculated stream- and equivorticity-lines are plotted in Figures 5.13 to 5.20. Streamlines for varied flow conditions, as obtained from experiments, are shown in Figures 5.21 and 5.22. These results are examined discussed in the following.

5.1 Velocity Profiles in the Core Region

Velocity profiles derived from equations 3.9 through 3.11 are plotted at planes through midpoints of ridges (a) and cavities (b) (as depicted in Figure 4.2) in Figures 5.1 through 5.9. Parabolic velocity profiles through a straight tube of diameter D (of the narrower bore) are superimposed for comparison. Figure 5.1a is for set 1 (Table 4.2) for which the ratio ϵ/γ (the cavity aspect ratio) is 0.619. That is, the depth of the cavity is ~ 1.64 times its width in the streamwise direction. The presence of the cavity does cause modifications to the velocity profiles in the spatially periodic geometry.

Calculated profiles for axial velocity versus radial position in Figure 5.1 were

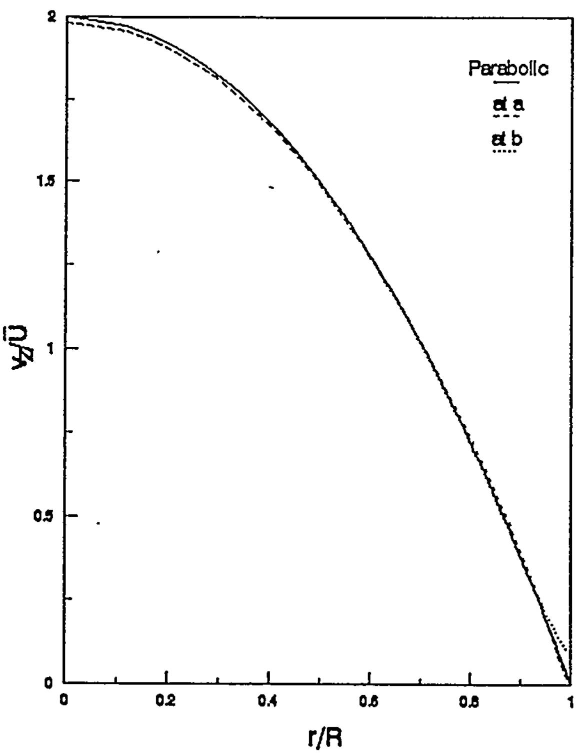

Fig.5.1a: Velocity Profiles for Set 1, Re=1.0

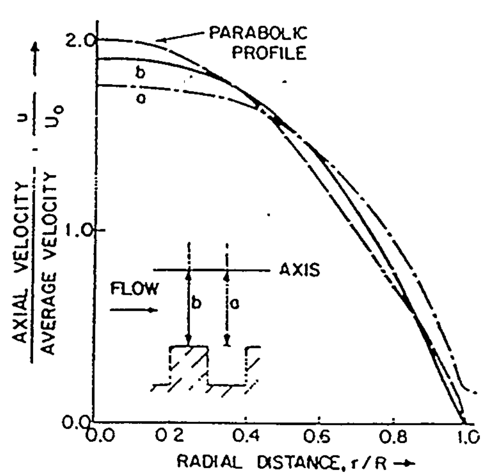

Fig. 5.1b: Experimental Velocity Profiles over the Center of a Ridge and a Recess for Re<0.2 [Jeje, 1985]

identical for Reynolds numbers of 0.5, 1.0 and 1.5, i.e. the flow rate did not effect any substantial changes in the pattern. On the ridge or protuberance, the velocity along the tube axis was less than for the parabolic profile. The two lines crossed twice as might be expected for the same volume rate, i.e. when continuity is satisfied. Over the cavity, the velocity pattern was nearly the same as over the ridge at the centre portion of the tube. At distance D/2 from the tube axis, the velocity was ~ 5% of the mean value as might be expected with re-circulation occurring inside the cavity. The profiles were however different quantitatively from the experimental results reported in Figure 3 by Jeje[1985] and reproduced in Figure 5.1b. Deviations from the parabolic profiles in the experimental results were more exaggerated even at Reynolds number < 0.2. Along the axis, over both ridge and the cavity, velocities were significantly lower than for Poiseuille flow and the deviation was larger, i.e. the core profile was flatter over the centre of the cavity than elsewhere in contrast to the present calculated results. The insensitivity of the velocity profiles to the flow rate or Reynolds number as suggested by the calculations were also not supported by experimental results[Figure 3b; Jeje, 1985]. Profiles were flatter near the axis as the Reynolds number increased.

A number of reasons can be suggested for the variance. One is that the conditions along the boundary of the calculation domain over the cavity could not be specified *a priori* and requires matching with solutions for the cavity region. Both the shear stress (proportional to the velocity gradient) and the local velocity have to assume the same values for the two regions which were overlapped. The overlapped region might have been too narrow, particularly since the core region did not extend any distance into the cavity region. That is, the points of separation and reattachment, the branch (or stagnation) points which are the corners of the step changes in the corrugated tube should have been totally immersed in both domains. It was also initially assumed that the velocity profiles were parabolic and fully developed 0.5 diameters of the narrower tube upstream of the test section and 0.5 diameters downstream. These were later modified to 2 and 5 diameters respectively. Any changes are not reflected in the velocity profiles plots. Due to the higher viscosity of the fluid and the low flow rates, the latter entrance and exit lengths are considered sufficient for the assumption of parabolic profiles at both boundaries. Calculations done on pressure drop suggests 1 diameter upstream and 3 diameters downstream were sufficient.

Other reasons for the differences may be due to inadequate grid sizing, the computational algorithm which may allow accumulation of indeterminate errors and the criteria for matching two overlapping domains. Nonetheless, calculations for the different geometrical configurations can be compared. Velocity profiles calculated for set 7 are shown for Re=1 in Figure 5.2. For this configuration, the cavity depth was ~ 3 times its width, which was identical to that for set 1 presented in Figure 5.1a. The calculated profiles were nearly identical to suggest that changes in the depth of the cavity did not affect the results. A slight increase in the width of the cavity (ϵ) without changes in the ridge width (δ) did effect a noticeable change in the profiles, in particular at $r/R \sim 0.8$ when deviations from the parabolic profile were obvious.

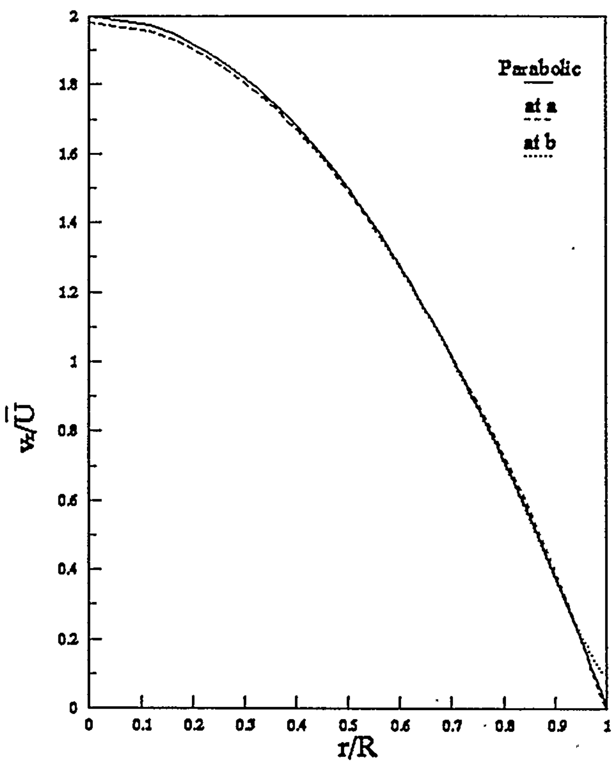

Fig. 5.2: Velocity Profiles for Set 7, Re=1.0

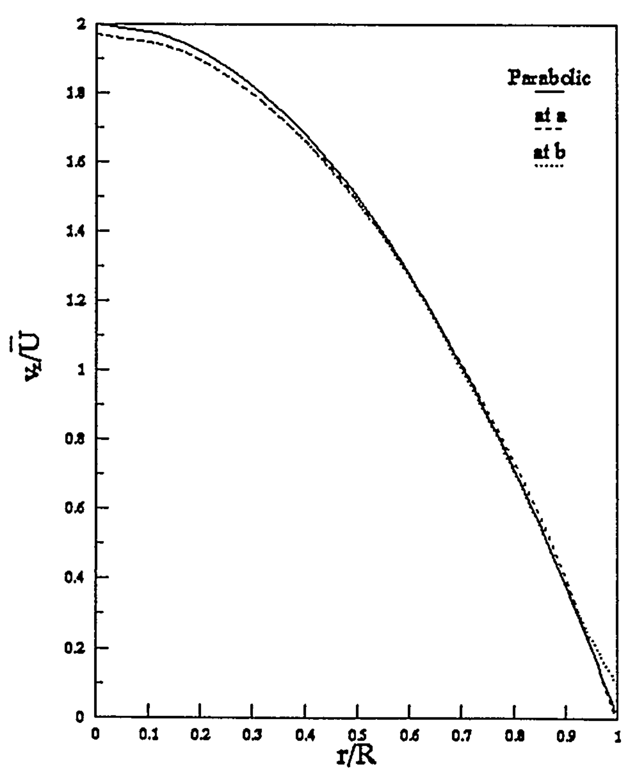

Fig. 5.3: Velocity Profiles for Set 5, Re=1.0

A comparison of the profiles for set 2 (ϵ/γ = 1.10) and set 1 is probably informative. For set 2, ϵ had increased by about 80% relative to set 1, all other dimensions remaining unchanged. Deviations from parabolic profile are significant for set 2 (Figure 5.4) in the tube core in reference to set 1 (Figure 5.1a). The cavity depths were similar for both cases. Velocity gradients at the walls were also different for the two sets; the gradient for set 1 being smaller than -4u/R for parabolic flow. The implications is that longer cavities allow for wider oscillations in the velocities nearer the wall but not in the core region.

Increase in the cavity length and a decrease in its depth as for sets 6 and 3 in Figure 5.5 and 5.6 respectively lead to profiles over the ridge and cavity being more distinct all the way to the tube axis. For set 4 (Figure 5.7), ϵ has been lengthened considerably and the velocity profiles show wide oscillations over a cycle of the corrugated tube. Set 8 in Figure 5.8, however, demonstrates that increasing aspect ratio ϵ/γ is not the only parameter forcing larger oscillations in the velocity field. The plots for this set are similar to that for set 3 in Figure 5.6. For set 8, the cavity depth is shallow but ϵ is the same as for set 3. For set 4, both the depth (γ) and cavity width (ϵ) were higher than for the two sets. This suggests that the cavity width exercises considerable influence on the flow patterns and may partially justify the use of λ/D (($\epsilon+\delta$)/D) by Dullien and Azzam[1973] for characterizing the flow. The depth in relation to the width of the cavity, nonetheless, determines the flow structures trapped in this region and the neglect of this scale on assuming similarity of flow patterns irrespective of the actual dimensions of ϵ, δ and γ are not supported

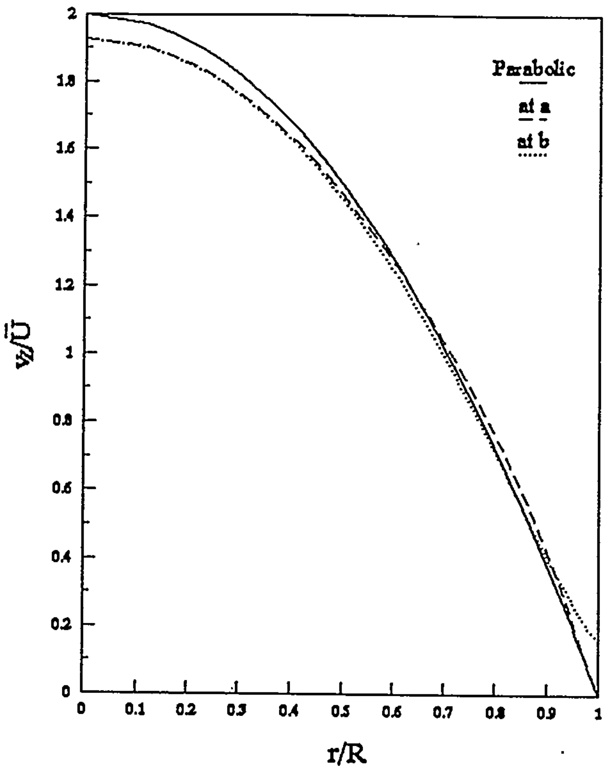

Fig. 5.4: Velocity Profiles for Set 2, Re=1.0

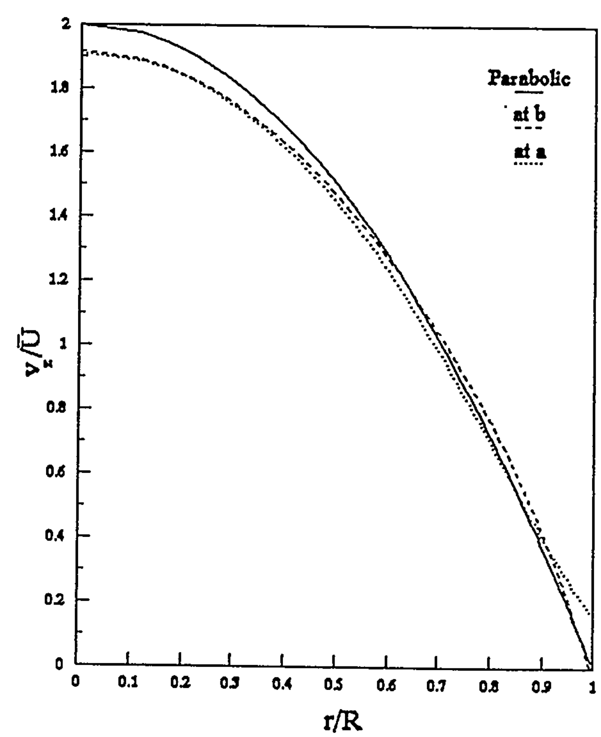

Fig. 5.5: Velocity Profiles for Set 6, Re=1.0

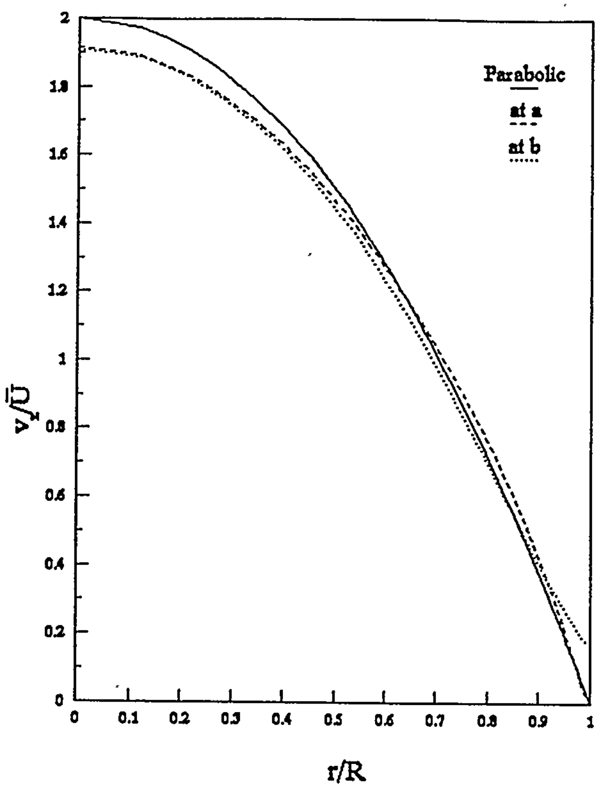

Fig. 5.6:Velocity Profiles for Set 3, Re=1.0

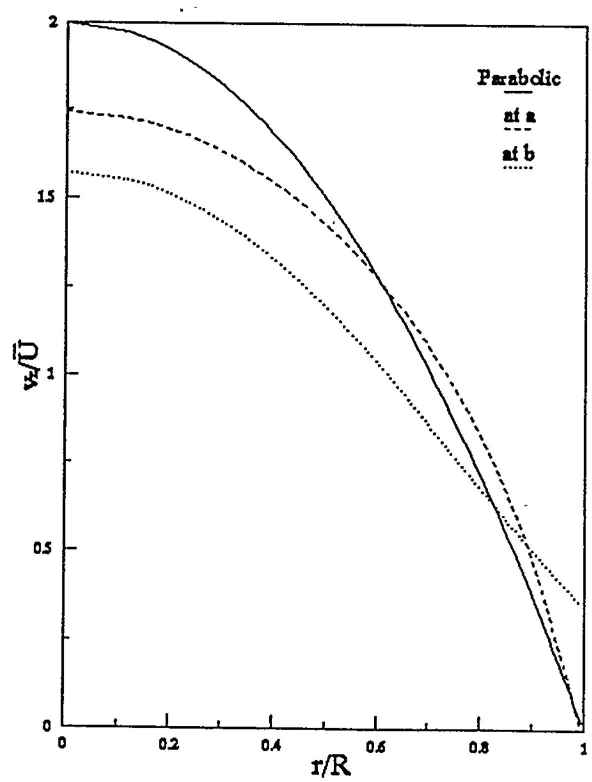

Fig. 5.7: Velocity Profiles for Set 4, Re=1.0

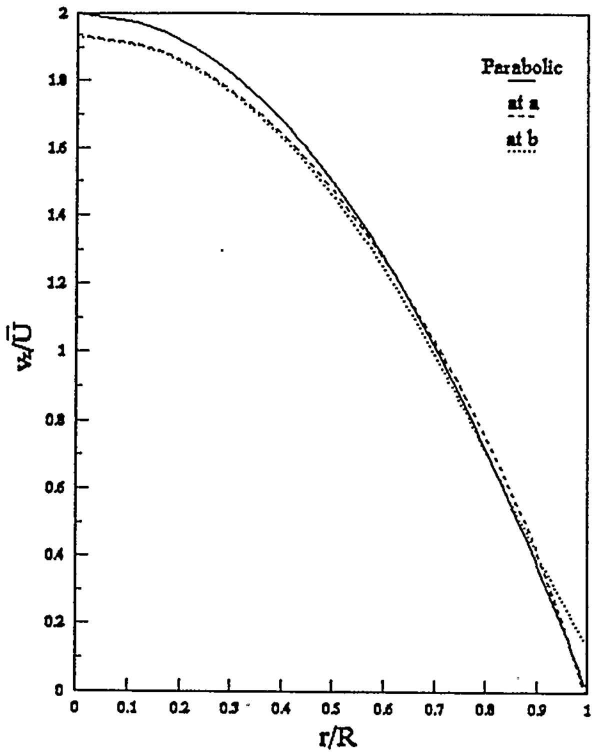

Fig. 5.8: Velocity Profiles for Set 8, Re=1.0

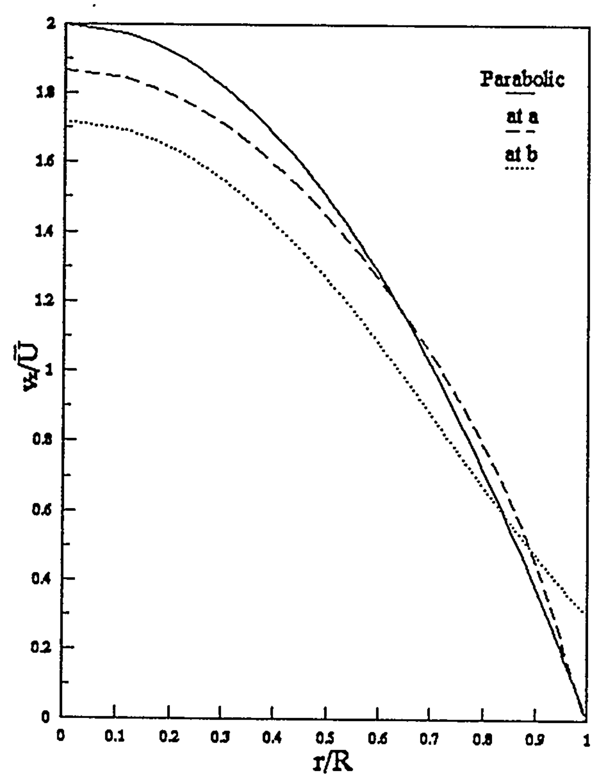

fig. 5.9: Velocity Profiles for Set 9, Re=1.0

by experimental observations.

Finally, the profile for tube configuration set 9 in Figure 5.9 can be compared with the other sets. For this arrangement, ϵ was long at almost 3 diameters of the narrow tube. The tube structure approximates a cascade of orifice plates in a tube under the slow flow conditions. The oscillations in the flow are similar to those for set 4 (Figure 5.7) but with lower deviations from the parabolic profile. Since the cavity depth (γ) for sets 4 and 9 were not very different, it is concluded that, over the long cavities for set 9, some recovery in flow has been achieved as was not as evident for set 4. Yet the oscillations persisted at a significant level compared with sets 1 and 2.

5.2 Axial Pressure Gradients

Plots of pressure gradients over a number of corrugation cycles as obtained from experiments are plotted in Figure 5.10 (a and b) versus Reynolds number (0 - 2) for the different arrangements. Each of the plots is a straight line as might be anticipated from a force balance on a steady flow through a straight, uniform-bore tube. For the latter, the relationship

$$\frac{\Delta p}{L} = 32\frac{\mu\bar{u}}{D^2} \qquad (5.1)$$

is obeyed. This is the Hagen-Poiseuille law. On re-arrangement of equation (5.1), one gets

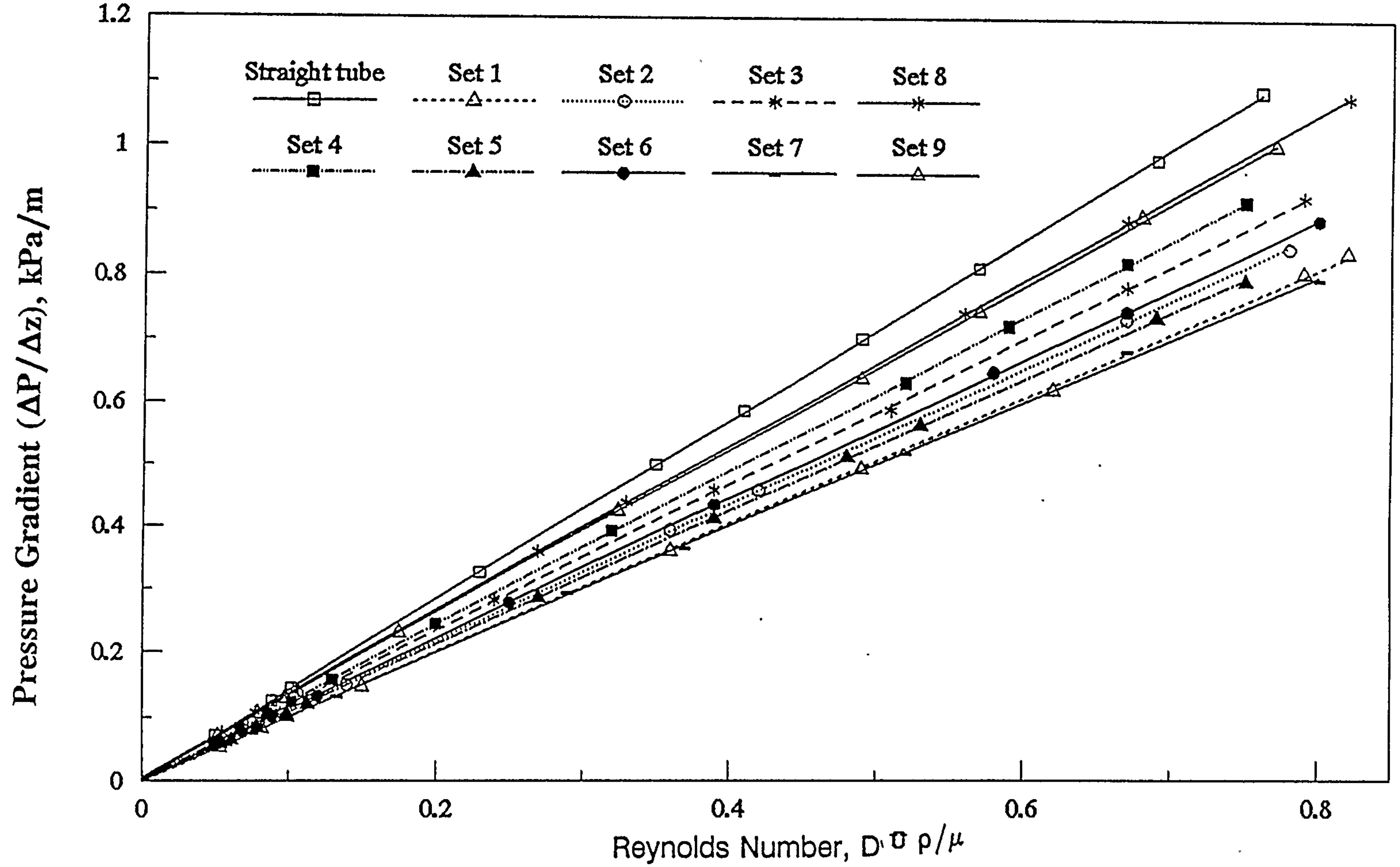

Fig. 5.10(a): Axial pressure gradients versus low (Re < 1) Reynolds number

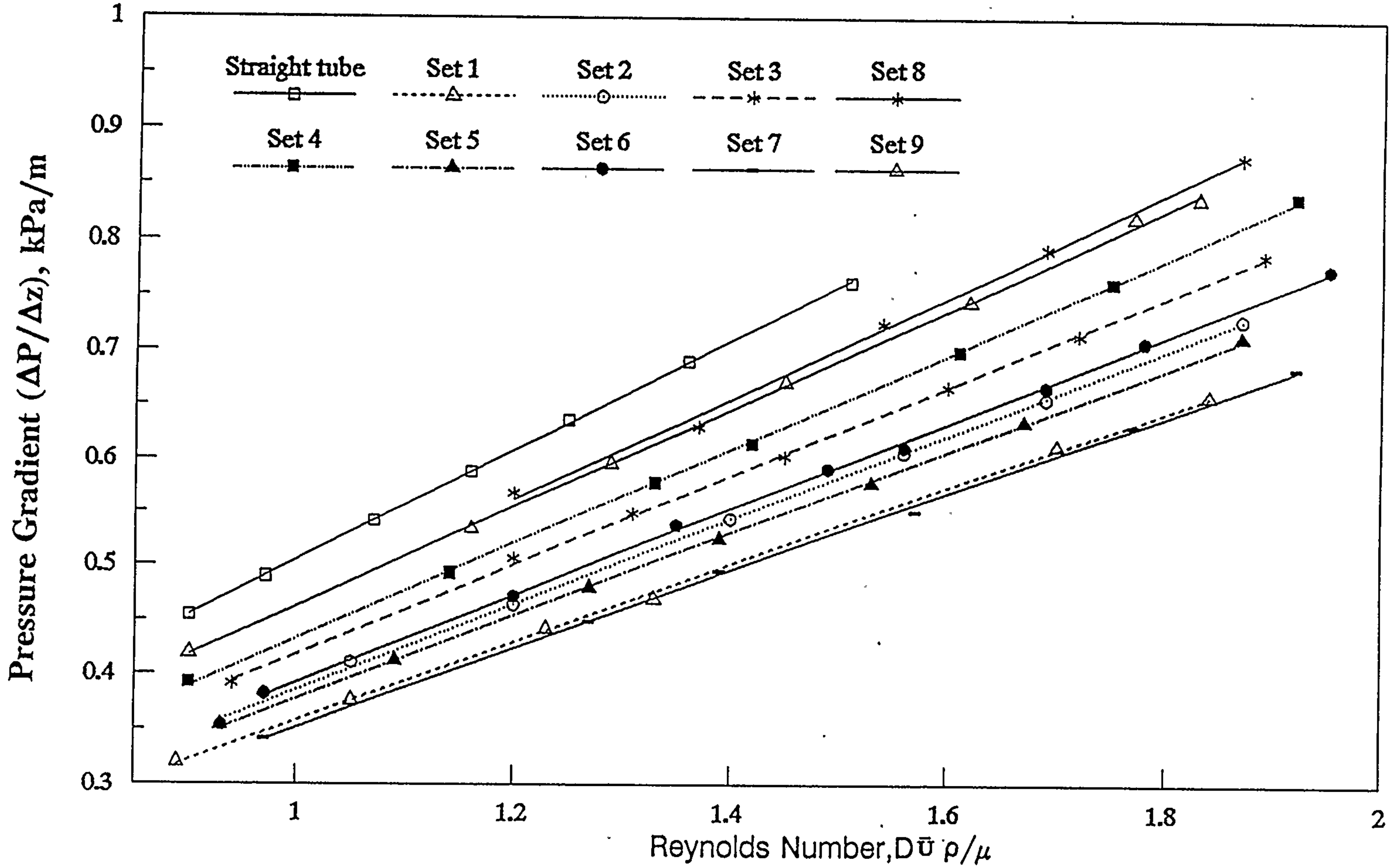

Fig. 5.10(b): Axial pressure gradients versus high (1 < Re < 2) Reynolds number

$$\frac{\Delta p}{L} = \beta\left(\frac{D\bar{u}\rho}{\mu}\right) ; \qquad \beta = \frac{32\mu^2}{D^3\rho} \tag{5.2}$$

where for a constant diameter (D) of the narrower tube of the configurations, β is a constant equivalent to a scaling parameter. A plot of $\Delta P/L$ versus Reynolds number then yields the slope β for a flow arrangement. Slopes lower than $(32\bar{u}^2/D^3\rho)$ suggest that there is drag reduction for the flow. Consequently, the value assigned to D - for the narrower tube, the wider tube or one based on volume averaging, assumes considerable significance for the claim of drag reduction. This issue has been mentioned earlier in the review of previous studies, in particular that of Dullien and Azzam[1973].

For the range of geometrical variations in this study, flow visualization experiments, show that streamlines at the outer edge of the core region did not penetrate significantly into the cavities except those which are relatively shallow (r ~ 0.05) and long, i.e. > 1 cm. That is, only for two of the sets (4 and 9) would any ambiguities arise. For set 8 with shallow cavity, errors on use of D or $(D+\gamma)$ are small. The stream tubes are therefore effectively defined by the diameter of the narrower tube. The results themselves provide justification.

Data for sets 1 and 7 show the largest drag reductions and these were similar even though the cavity depth (γ) for set 7 is almost double that for set 1, all other parameters remaining unchanged. The next level of drag reduction was exhibited by set 5 with ϵ/γ which is intermediate between values for the other two foregoing. This set, however, has a slightly wider cavity then for both. Set 2 followed in the sequence. However, sets 3, 6 and 8 with the same $\delta/(\delta+\epsilon)$, a characteristic ratio used by Dullien and Azzam[1973, 1977], equal to 0.329 showed different drag reductions. The primary difference for the three were the cavity depths (γ). Of the three, set 6 with the largest γ also has the most drag reduction followed by set 3. But the shallow cavity set (8) exhibits the least drag reduction of all the sets. In the data, sets 2 and 6, inspite of significant differences in γ but with similar ϵ, showed similar levels of drag reduction. That is, what is responsible for lowering the frictional resistance to the flow is a combination of the absolute lengths for ϵ, δ and γ as they determine the flow structures in the cavities and the ratio of the lengths in combination with the tube diameter, not a simple geometric similarity as suggested in earlier studies.

The results have been re-plotted in terms of friction factor f, defined as

$$0.5f\left(\frac{D\bar{u}\rho}{\mu}\right) = 32\ ; \qquad f = \left(\frac{\Delta P}{1/2\rho\overline{u^2}}\right)\left(\frac{D}{L}\right) \tag{5.3}$$

versus Reynolds number on Figures 5.11 (a and b). The constancy of the left side equation (5.3) at different Reynolds numbers is more clearly shown in Figure 5.12. The scatter of experimental results is random and less than 2%. Figure 5.12 shows that the configuration in set 7 leads to a reduction in friction factor of ~ 30% at the low Reynolds number studied. Such a dramatic improvement in reducing drag will be of course beneficial to maintaining the ascent of sap in living plants in which such structures are sometimes observed.

Results from numerical calculations are presented in Table 5.1 for comparison

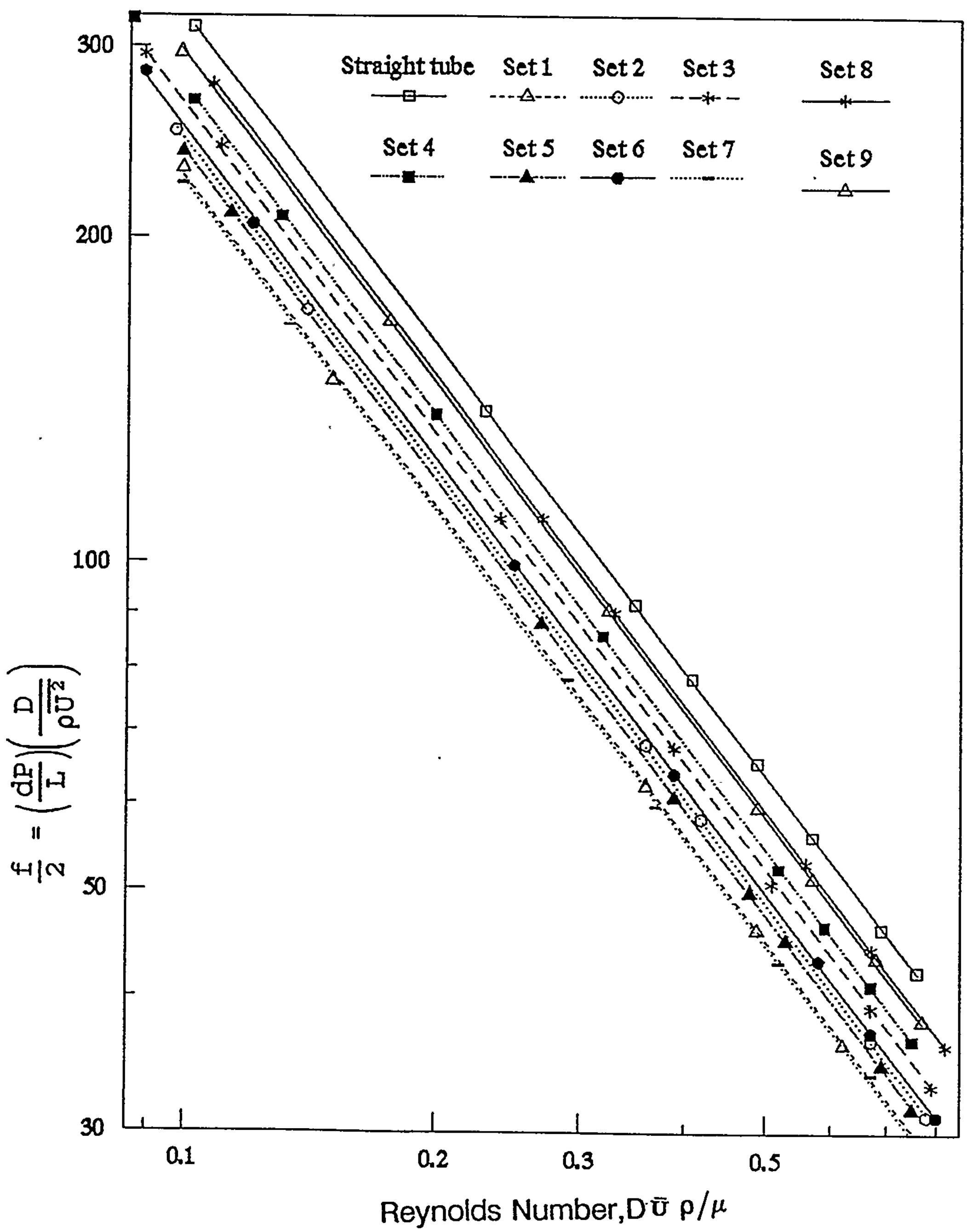

Fig. 5.11(a): Variation of dimensionless pressure gradients versus low (Re < 1) Reynolds number

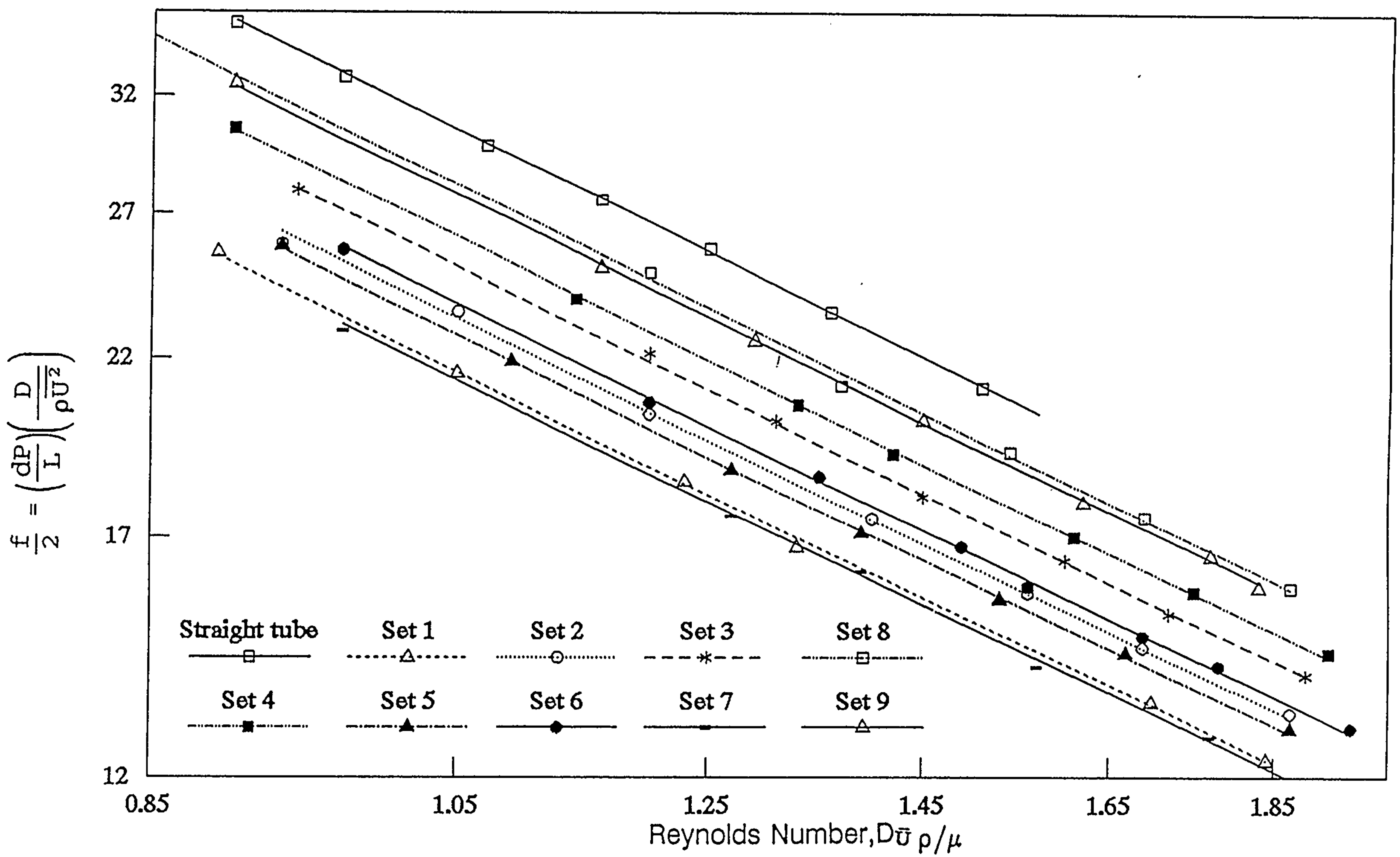

Fig. 5.11(b): Variation of dimensionless pressure gradients versus high (1 < Re < 2) Reynolds number

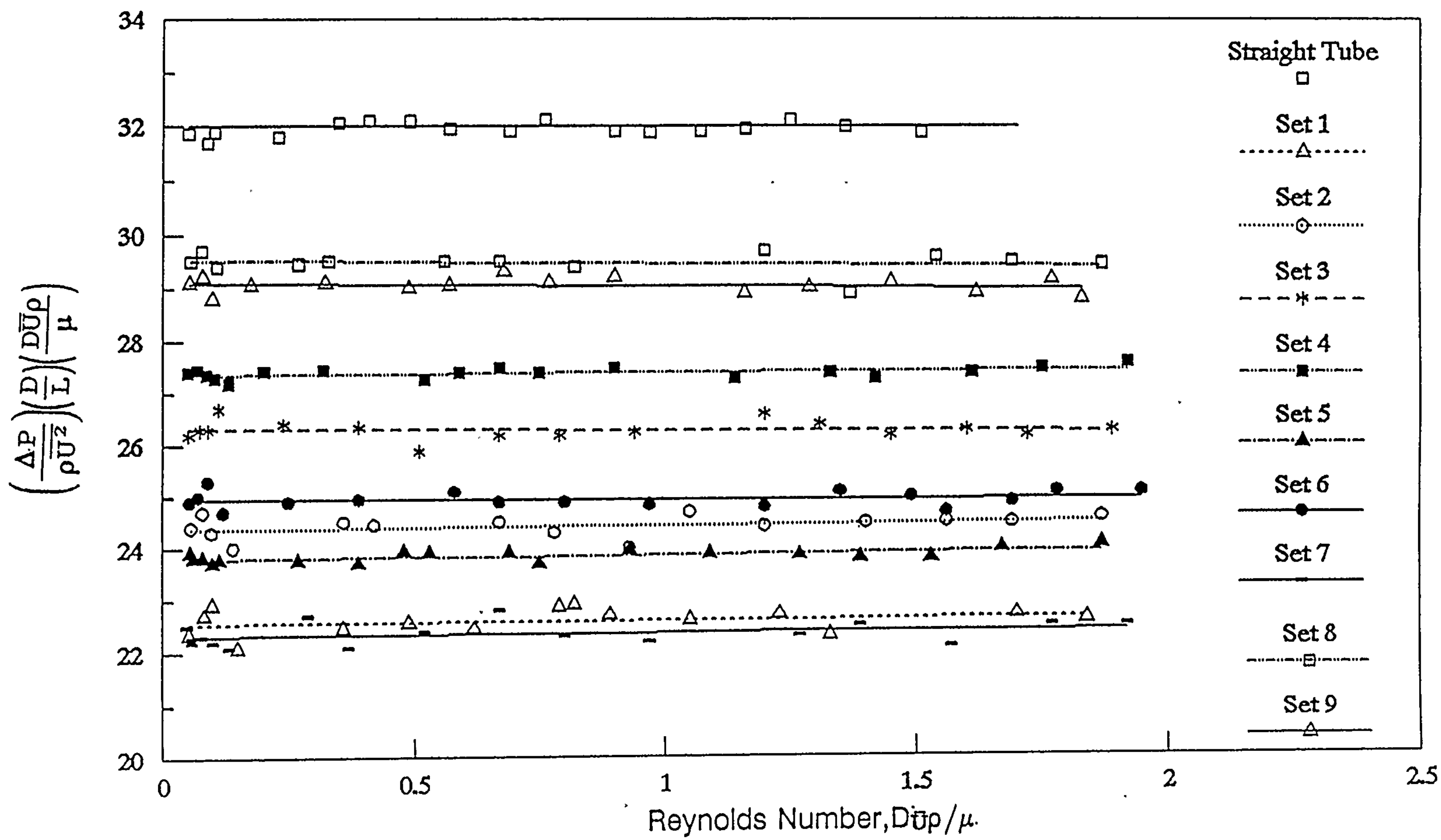

Fig. 5.12: Variation of $\left(\frac{\Delta P}{\rho \overline{U}^2}\right)\left(\frac{D}{L}\right)\left(\frac{D\overline{U}\rho}{\mu}\right)$ versus Reynolds number

with experimental data. The predictions show drag reductions which are both smaller than from experiments and not in the same order. Set 4, for example, shows the lowest drag reductions from numerical calculations. Issues associated with the simulation still have to be resolved.

5.3 Streamline and Equivorticity Contours

5.3.1 Computational Results

Streamlines and equivorticity contours calculated from numerical simulation are shown in Figures 5.13 to 5.21. The plots in Figure 5.13 are for the tube configuration of set 1. Streamlines show a counter-clockwise circulation in the cavity. The ring vortex formed is symmetric about the mid-plane through the cavity and the streamlines in the core region are indented towards the recess. The structures are similar to those reported for single cavities in works by Higdon[1985, 1990] and others. The streamline which divide the two regions of flow (core and cavity), however, seems to separate and reattach at points which do not correspond to the corners or true stagnation points.

The contour of vorticity shows radially inwards (towards the tube axis) increasing values with the highest vorticity near the branch points as one would anticipate. Along the midplane through the cavity perpendicular to the tube axis, highest vorticity occurred outside the cavity in the region of closepacked streamlines. The "eye" of the streamlines within the cavity did not correspond to where the vorticity is highest. Vorticity was also low at distances deeper than the cavity width,

Table 5.1: Experimental and Calculated Pressure Gradients

Tube Arrangement	Experimental (0.5f)Re	Caculated (0.5f)Re
Set 1	22.50	30.50
Set 2	24.43	28.95
Set 3	26.25	28.47
Set 4	27.43	24.34
Set 5	23.85	30.18
Set 6	25.12	28.46
Set 7	22.28	30.50
Set 8	29.40	29.10
Set 9	29.05	26.85

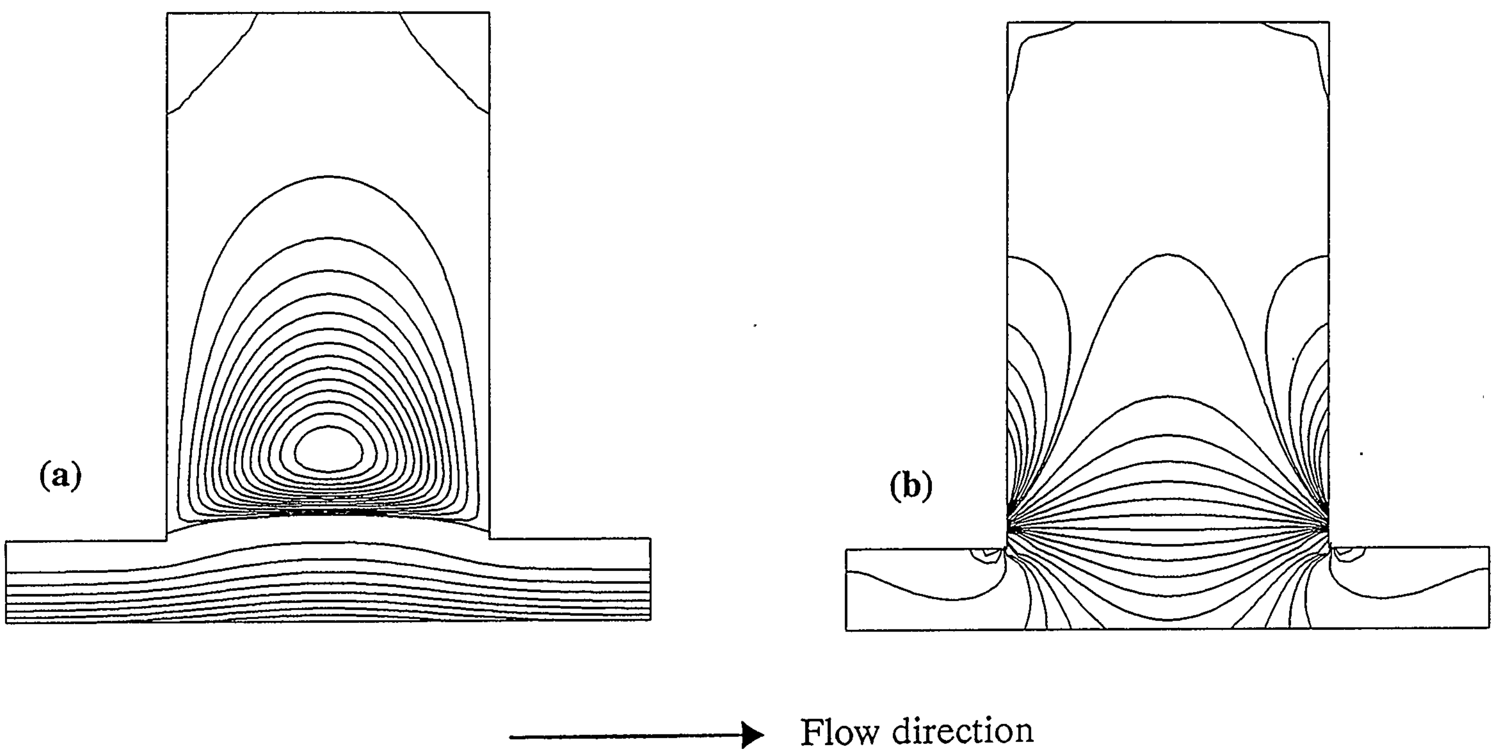

Fig. 5.13: (a) Stream function and (b) vorticity contour map for set 1, Re=1.0

from the mouth.

The plots were similar to the above for set 7 which exhibited the highest drag reduction of all the tube configurations investigated. Calculations predict that a second weak vortex exists deeper in the cavity, starting about one cavity width inside the recess. The pattern of vorticity distribution is similar also for sets 1 and 7.

Sets 2 and 5, the next most efficient configuration for drag reduction, showed similar patterns to sets 1 and 7 respectively. For cavities whose depth are of the order of the width, one large circulation is noted. When the depth is of the order of twice the width or more, other vortices are predicted in the cavity as have been predicted and observed by Friedman[1970], Pan and Acrivos[1967], Bozeman and Dalton[1973], Mehta and Lavan[1969] and others for flow over single open or closed cavities.

Deviations from the above start to appear as the cavity width is made larger. For set 6, shown in Figure 5.17, the streamlines in the cavity have two "eyes" or centres of circulation. The cavity depth (γ) is shallower than the width (ϵ) and rotating flows occur around both eyes. The flow pattern is symmetric about the midplane through the cavity to suggest that inertial effects are neither substantial inside and at the open surface of the cavity. That is, the flow is predicted to be reversible at Reynolds number < 2. A line of zero vorticity divides the cavity into two zones with opposite signs for the parameter. Extrema for vorticity are not within the cavity space but at the walls. The above patterns are the same for set 3 but in an exaggerated form. For this set, only the cavity depth is shallower than for set 6.

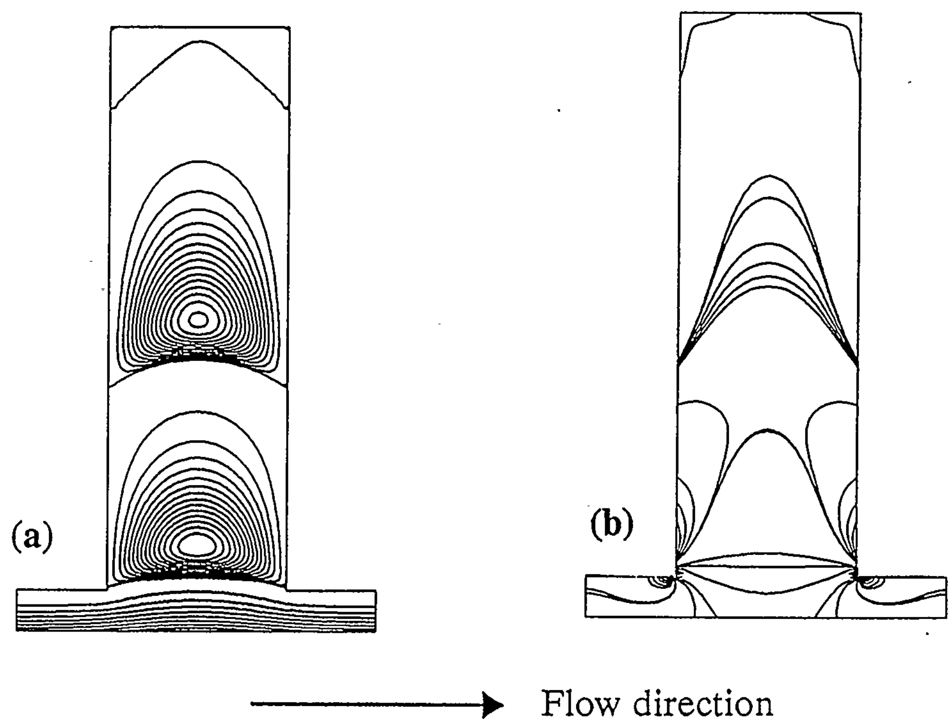

Fig. 5.14: (a) Stream function and (b) vorticity contour map for set 7, Re=1.0

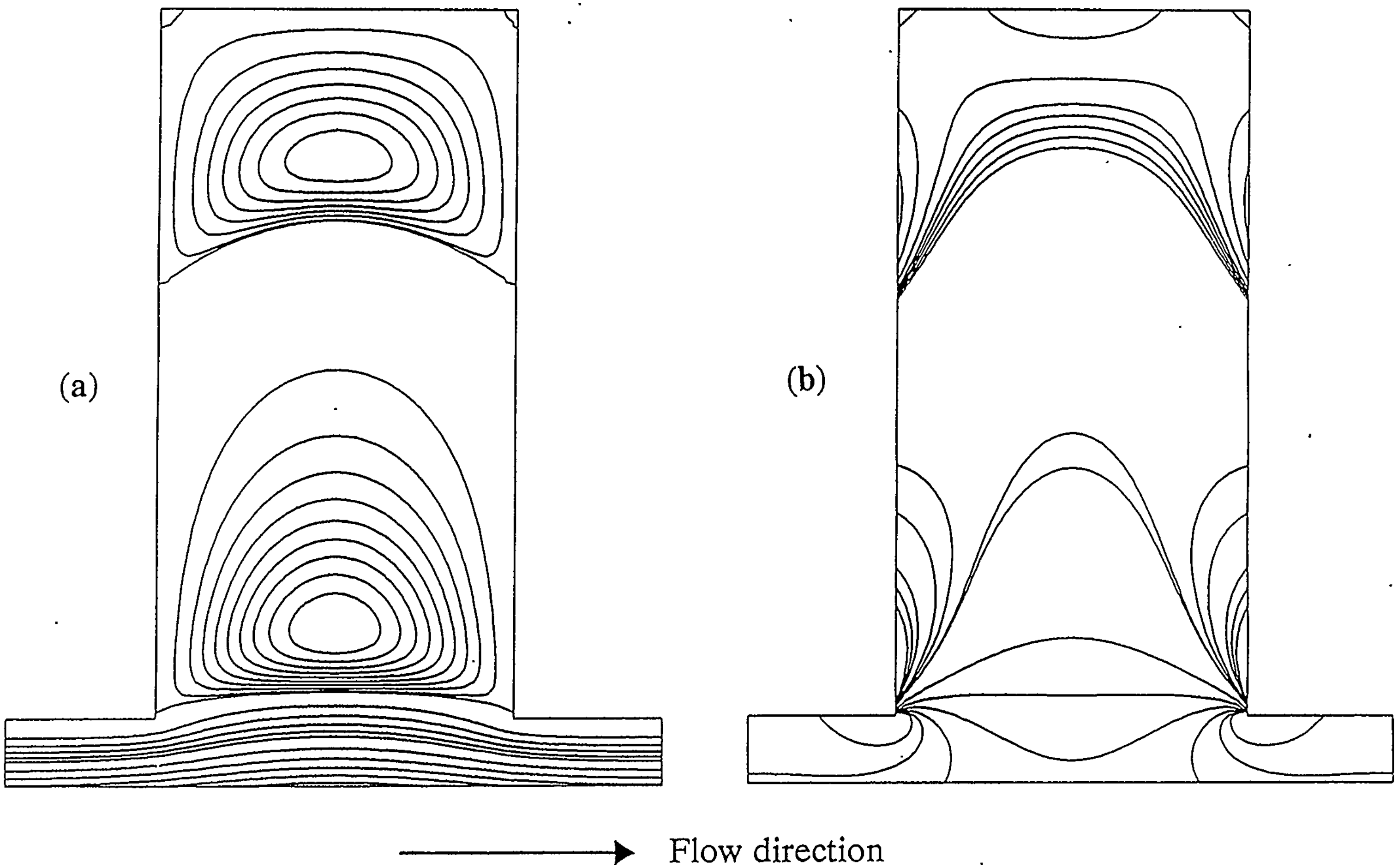

Fig. 5.15: (a) Stream function and (b) vorticity contour map for set 5, Re=1.0

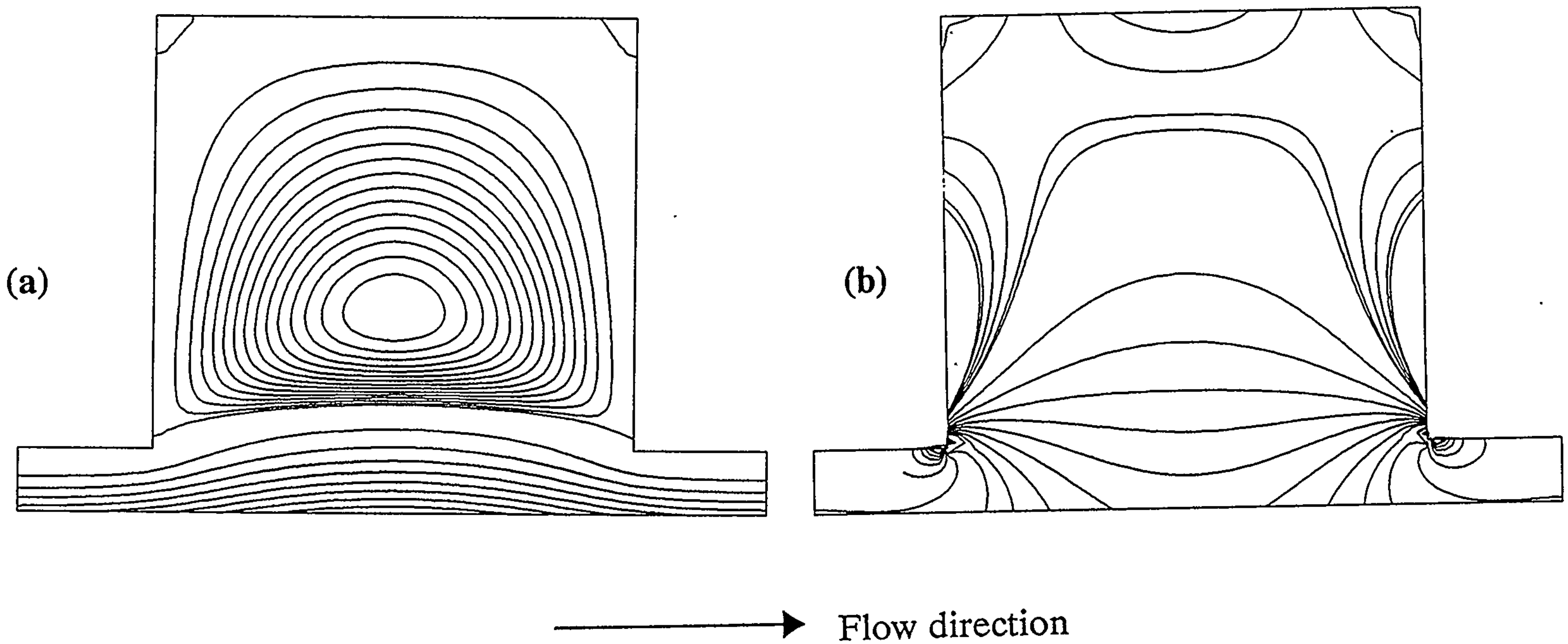

Fig. 5.16: (a) Stream function and (b) vorticity contour map for set 2, Re=1.0

Streamlines from the "outer" flow penetrated deeper into the cavity but no branch points existed at the distal cavity wall.

As the cavity width to depth ratio (ϵ/γ) was further increased, two separate vortices are predicted as illustrated with set 4 in Figure 5.19. Streamlines would then penetrate to the distal wall and an attachment and a separation point would each exist at this wall. The cavity depth for this configuration is greater than for set 3 (Figure 5.18) for which the vortices had not become isolated. Thus the absolute cavity width (ϵ), in some relationship to depth, determines the flow structures that will emerge. Results for set 8 with very shallow depth (Figure 5.20) are simply the same form as for set 4. Small vortices are trapped at the corners. A similar structure can be anticipated for set 9 which has the highest aspect ratio (ϵ/γ).

From the foregoing, it may be suggested that drag reduction is effected by thecirculatory flows in the cavity acting as ball-bearings for the core flow. Single vortices at the inlet to the cavity are apparently more efficient if the calculation results can be compared with experimental data for pressure drop. A comparison with the results of numerical simulation for pressure drop would suggest that the configuration in set 4 for which two vortices were incipient is most efficient while the other structures lead to less efficient flows. The discrepancy and the symmetry always observed with the calculations, i.e. negligible inertia, are attributed to difficulties associated with the calculations as earlier described.

(a)

(b)

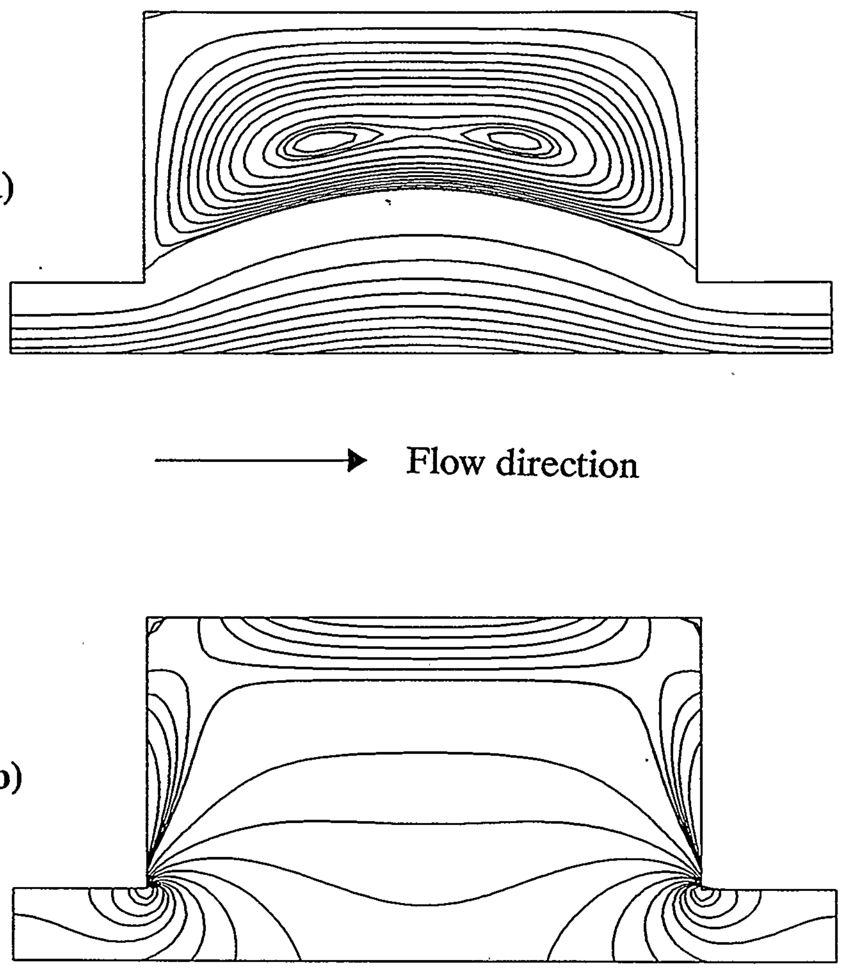

Fig. 5.17: (a) Stream function and (b) vorticity contour map for set 6, Re=1.0

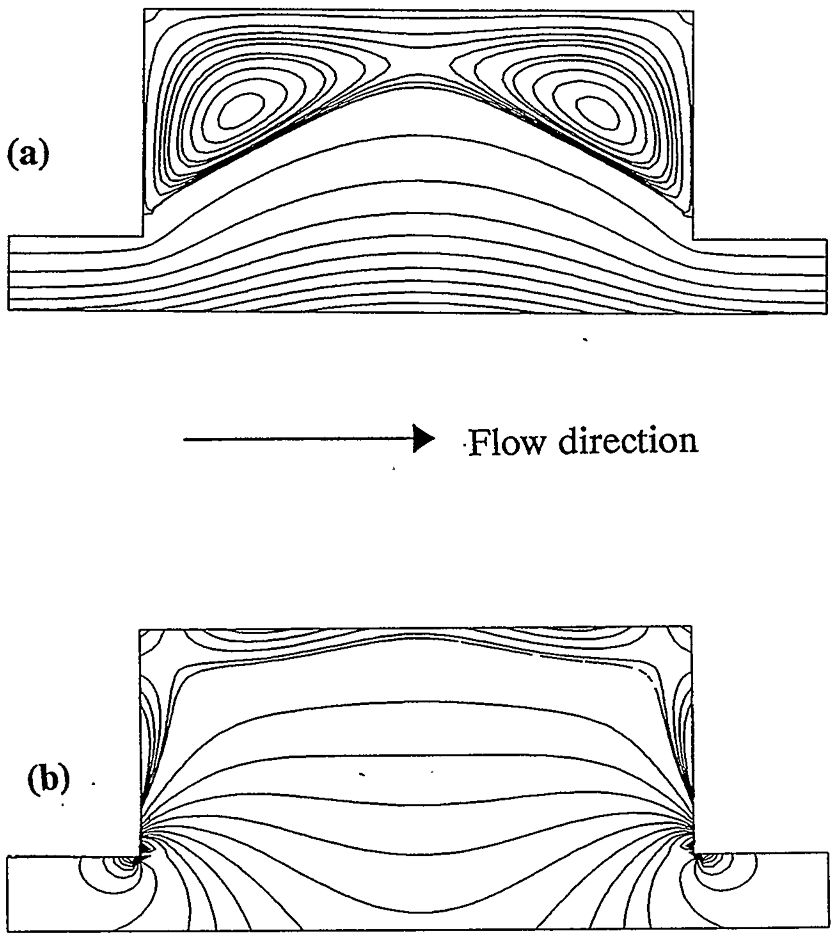

Fig. 5.18: (a) Stream function and (b) vorticity contour map for set 3, Re=1.0

(a)

(b)

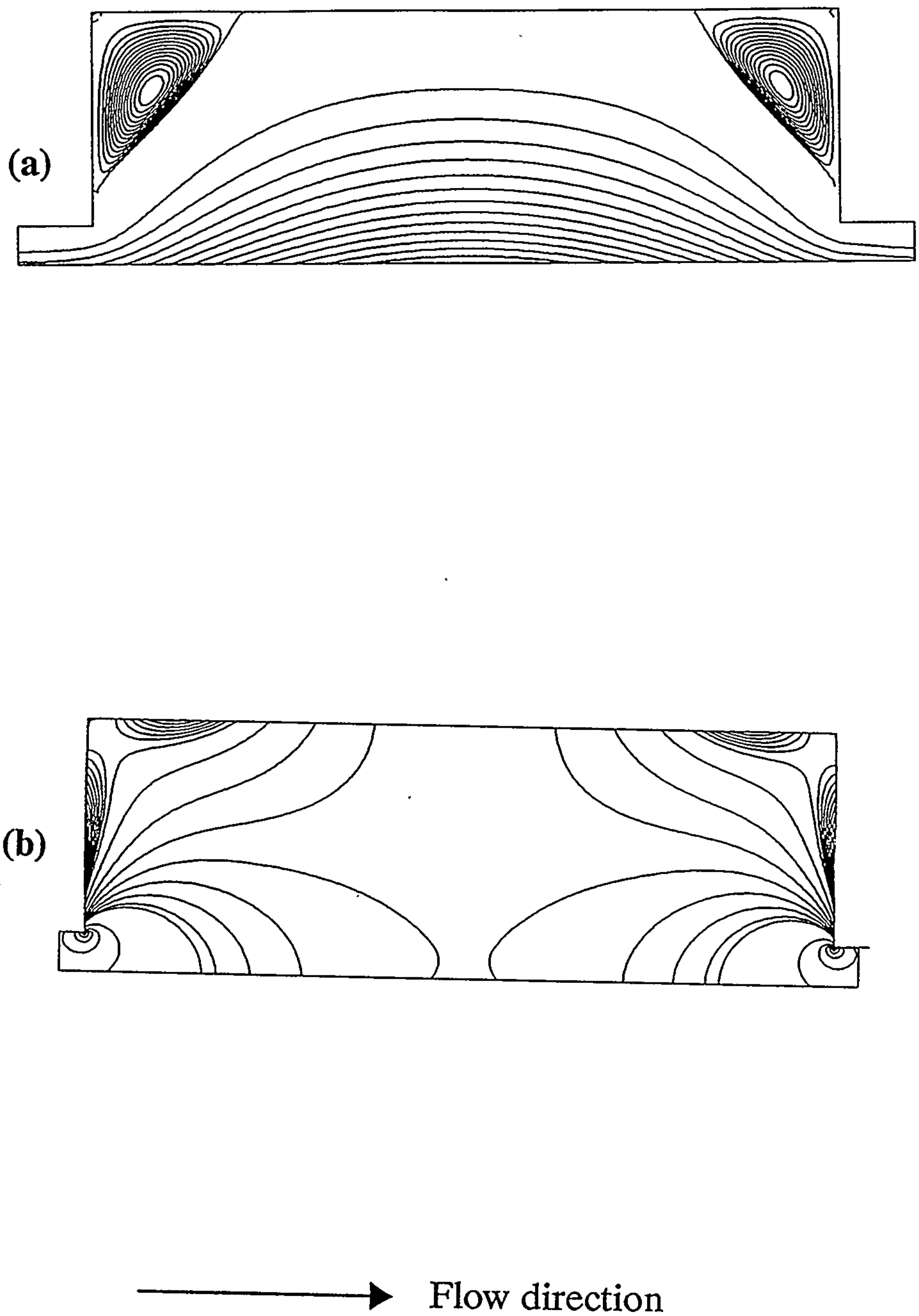

Fig. 5.19: (a) Stream function and (b) vorticity contour map for set 4, Re=1.0

(a)

(b)

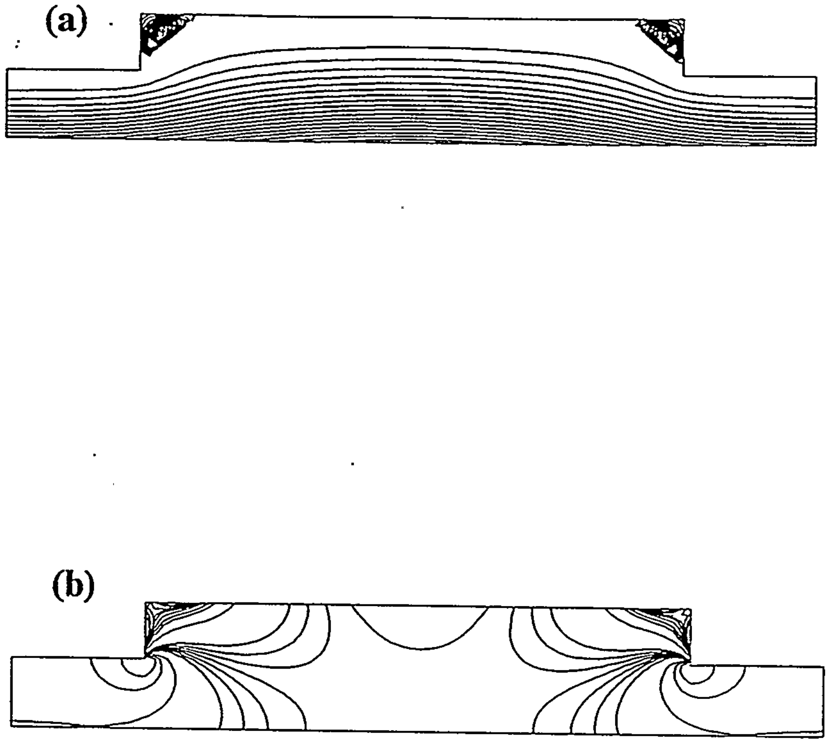

Flow direction

Fig. 5.20: (a) Stream function and (b) vorticity contour map for set 8, Re=1.0

5.3.2 Experimental Observations

Visualization of the flow patterns through recording the stream paths of some tiny hydrogen bubbles generated in the flow stream is, as earlier described, based on streak photography. For laminar flow, the lines of the photographic images are also the streamlines when the flows are steady and the frame reference or observation point is stationary[Lugt, 1983; Tritton, 1983]. The region of observation is confined to the cavities and the neighbourhood of the ridges, i.e. the wall region for the core flow. Bubbles which move through the field of view in the axial direction and the flow trapped within the cavities are expected to describe the paths of motion of the liquid itself as long as the bubbles were sufficiently small and the population density was low to preclude interference. The location of the filament for generating bubbles was sufficiently displaced from the observation site (at least 10 cm) and enough time was given between the start of the flow and recording of images that velocity deficits between a bubble and the liquid immediately around it are expected to be negligible[Clayton and Massey, 1967; Wilkinson and Willoughby, 1981]. In regions of low velocities (< 0.1 mm/s) within the cavity, buoyancy is still important and "streamlines" may appear not to close as a tracer bubble is displaced to a different orbit. This behaviour were observed for long exposures and very slow flows of the glycerine-water mixture through the corrugated tubes. Tracks of the hydrogen bubbles, nonetheless, provide information about the number, size and asymmetries of the vortices in the recesses and the streamlines which bound the open cavities. These are presented in the following.

Photographic images for the streamline patterns for set 7, the tube configuration arrangement with the lowest drag, are shown in Figure 5.21 at Reynolds number of unity (1) for the core flow. Only one vortex, near the cavity entrance, could be observed and this was nearly symmetric about the midplane (orthogonal to the tube exit) through the cavity. The streamlines at the mouth were only slightly asymmetric, showing a steeper slope at the upstream end than for the downstream. The importance of adequately aligning the tubes is demonstrated in Figure 5.22. Here, the downstream ring was slightly misaligned so that, in the field of view, the ridge downstream was ~ 1mm shorter than the ridge upstream.The vortex in the cavity was significantly skewed. In general, the features are qualitatively the same as for the numerical calculations for the same tube in Figure 5.14. The flow patterns for set 1 were, as expected similar to that for set 7.

For set 2 (Figure 5.23), three pictures are presented for core flow at Reynolds numbers of 0.5, 1.0 and 1.51. The flow structures are similar for all the Reynolds numbers and in comparison with calculated results for this arrangement (Figure 5.15). The vortices and streamlines at the mouth show slight asymmetries even at Reynolds number of 0.5.

Set 6 in Figure 5.24 at Re=1.0, as was predicted from calculations (Figure 5.17), shows two centres of circulation circumscribed by streamlines through the rest of the cavity. The same structures are apparent at a Reynolds number of 0.5 (Figure 5.24b) even though most of the streamlines were not closed because exposure time was too short.

In the series of tube configurations, set 3 has the next wider cavity. At Reynolds number of 1.0, as is shown in Figure 5.25, two centres of circulation form within the cavity and these were larger and wider separated than for set 6 under similar flow conditions. Streamlines from the outer flow penetrated significantly into the cavity but did not reach the wall to form branch points. Similar patterns were also observed at Reynolds number of 0.5 and 1.5.

As the cavity length was further increased (set 4) , the streamlines from the cavity mouth penetrated to the distant walls in agreement with predictions from computations. Two vortices were trapped in the corners of the recess away from the main flow.

It is concluded from the foregoing that the experimental observations and calculated streamlines are in qualitative agreement. For the two, small difference exist in the shapes of the contours near the entrance to the cavities and since values for the stream function were not derived from the observations, it is not possible to compare numerically the degree of variation and at which locations the deviations are significant. Only a partial success is claimed for the simulation consequently.

Figure 5.21: Streamlines (or pathlines of tiny hydrogen bubbles) in and at the mouth of a cavity for set 7 (ϵ = 0.238 cm, γ = 0.748 cm, δ = 0.239 cm and D = 1.97 cm); Re = 1.0 [Top]

Figure 5.22: Streamlines (or pathlines of tiny hydrogen bubbles), for slightly misaligned ring, in and at the mouth of a cavity for set 7 (ϵ = 0.238 cm, γ = 0.748 cm, δ = 0.239 cm and D = 1.97 cm); Re = 1.0 [Bottom]

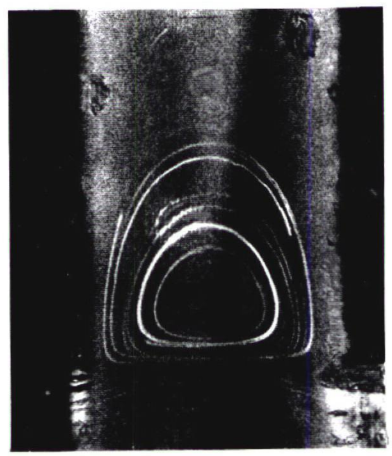

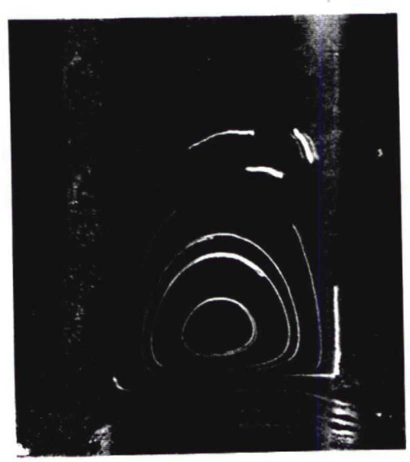

Figure 5.23a: Streamlines (or pathlines of tiny hydrogen bubbles) in and at the mouth of a cavity for set 2 (ϵ = 0.428 cm, γ = 0.389 cm, δ = 0.239 cm and D = 1.97 cm); Re = 0.5 [Top]

Figure 5.23b: Streamlines (or pathlines of tiny hydrogen bubbles) in and at the mouth of a cavity for set 2 (ϵ = 0.428 cm, γ = 0.389 cm, δ = 0.239 cm and D = 1.97 cm); Re = 1.0 [Middle]

Figure 5.23c: Streamlines (or pathlines of tiny hydrogen bubbles) in and at the mouth of a cavity for set 2 (ϵ = 0.428 cm, γ = 0.389 cm, δ = 0.239 cm and D = 1.97 cm); Re = 1.5 [Bottom]

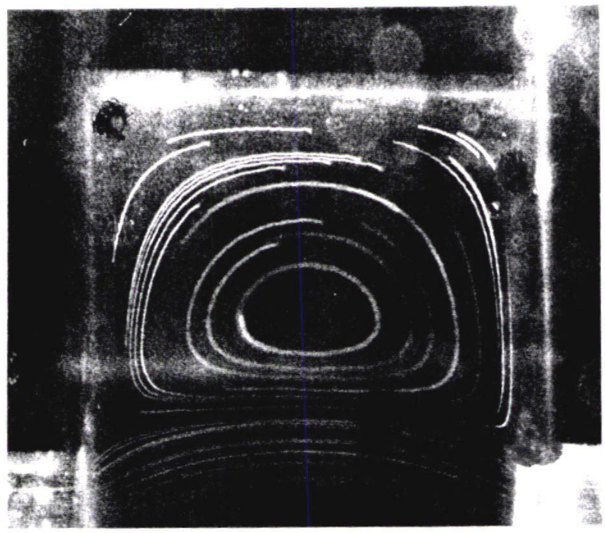

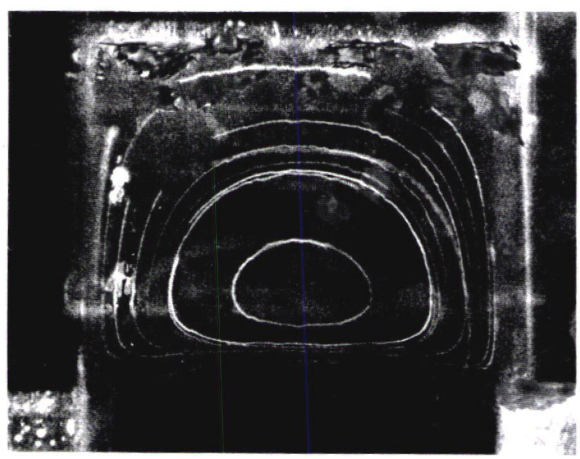

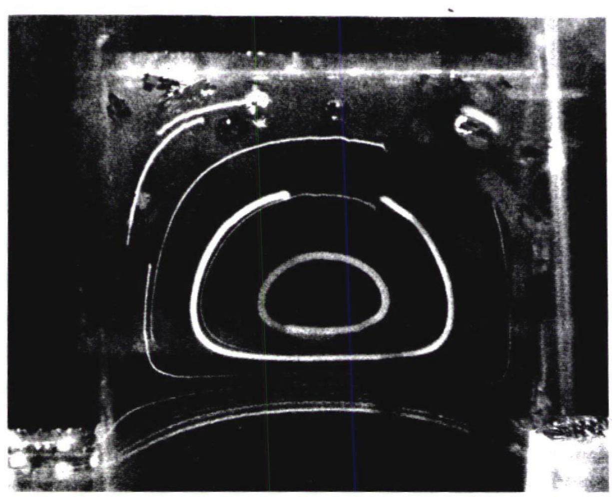

Figure 5.24a: Streamlines (or pathlines of tiny hydrogen bubbles) in and at the mouth of a cavity for set 6 ($\epsilon = 0.487$ cm, $\gamma = 0.239$ cm, $\delta = 0.239$ cm and D = 1.97 cm); Re = 0.5 [Top]

Figure 5.24b: Streamlines (or pathlines of tiny hydrogen bubbles) in and at the mouth of a cavity for set 6 ($\epsilon = 0.487$ cm, $\gamma = 0.239$ cm, $\delta = 0.239$ cm and D = 1.97 cm); Re = 1.0 [Middle]

Figure 5.25: Streamlines (or pathlines of tiny hydrogen bubbles) in and at the mouth of a cavity for set 3 ($\epsilon = 0.487$ cm, $\gamma = 0.198$ cm, $\delta = 0.239$ cm and D = 1.97 cm); Re = 1.0 [Bottom]

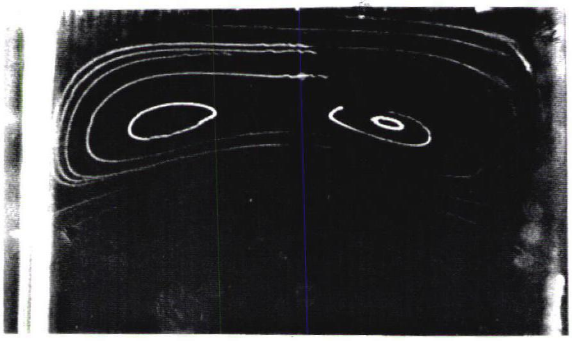

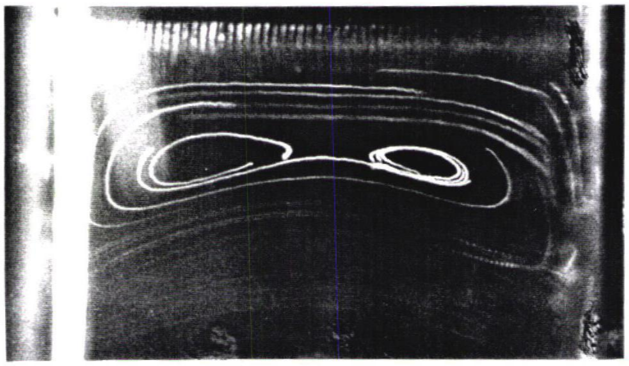

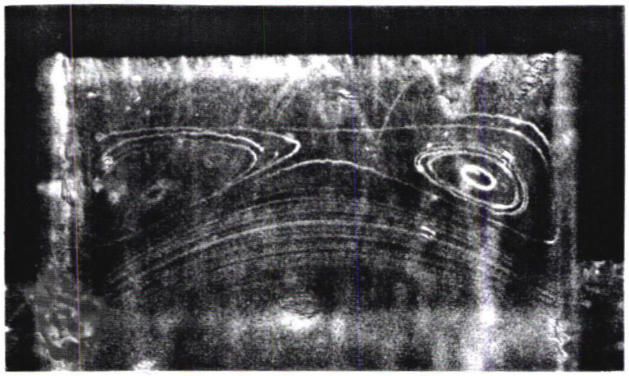

6. CONCLUSIONS AND RECOMMENDATIONS

Conclusions

The following are concluded from this study:

From experiments performed with nine types of cavity configurations, the cavity with aspect ratio (width/depth) of 0.3-0.6 and ridge to recess width ratios of ~ 1 showed the highest drag reduction.

Both the calculated streamlines and those observed through pathlines of tiny hydrogen bubbles are in qualitative agreement.

Calculated velocity profiles showed spatial oscillations through different planes over a cycle of corrugation. Configurations with wider cavities showed a maximum deviations from the parabolic profile through a tube of the same diameter as the narrower segment along the flow path.

Recommendations

A few recommendations can be made towards improving the existing experimental procedure, and the study of flow through internally corrugated tube in general:

The Reynolds number could be increased to extend the range for the study of the flow behaviour and patterns in the cavity.

Cinematography rather than still pictures will improve the visualization of the dynamic progression of the flow structure.

Instead of using hydrogen bubbles as the flow visualization technique, other techniques such as Laser-Doppler anemometry may be employed.

REFERENCES

Azzam, M.I.S. and F.A.L. Dullien: "Flow in tubes with periodic step changes in diameter: a numerical solution", Chem. Eng. Sci., **32**, 1445, (1977).

Batra, V.K.: *Laminar Flow Through Wavy Tubes and Wavy Channels*, M.A.Sc. Thesis, University of Waterloo, Waterloo, Canada (1969).

Batra, V.K., G.D. Fulford and F.A.L. Dullien: "Laminar flow through periodically convergent-divergent tubes and channels", Can. J. Chem. Eng., **48**, 622, Dec., (1970).

Bird, R.B., et al.: *Transport Phenomena*, Wiley International Edition, Tokyo, Japan, (1960).

Bozeman, J.D. and C. Dalton: "Numerical study of viscous flow in a cavity", J. Computat. Phys., **12**, 348, (1973).

Brandeis, J. and J. Rom: "Three-layer interactive method for computing supersonic laminar separated flows", AIAAJ, **18**, no. 11, 1320, Nov., (1980).

Brandeis, J. and J. Rom: "Interactive method for computation of viscous flow with recirculation", J. Computational Phys., **40**, 396, (1981).

Cheng, R.T.: "Numerical solution of the Navier-Stokes equations by the finite element method", Phys. Fluid, **15**, no. 12, 2098, Dec., (1972).

Christiansen, E.B., S.J. Kelsey and T.R. Carter: "Laminar tube flow through an abrupt contraction", AIChEJ, **18**, no. 2, 372, (1972).

Clayton, B.R. and B.S. Massey: "Flow visualization in water: a review of techniques", J. Sci. Instrum., **44**, 2, (1967).

CRC Handbook of Chemistry and Physics, 63rd Edition, 1982-1983, p. D-239.

Dullien, F.A.L. and V.K. Batra: "Determination of the structure of porous media", Ind. Eng. Chem, **62**, 25 (1970).

Dullien, F.A.L. and M.I.S. Azzam: "Flow rate-pressure gradient measurements in periodically nonuniform capillary bore", AIChE Journal, **19**, no. 2, 222 (1973).

Friedman, M.: "Flow in a circular pipe with recessed walls", J. Appl. Mech., Trans. of ASME, 5, March, (1970).

Gaudet, L.: "An assesment of the drag reduction properties of riblets and the penalties of off design conditions", RAE Tech. Memo Aero., 2113, (1987).

Higdon, J.J.: "Stokes flow in arbitrary two-dimensional domains: shear flow over ridges and cavities", J. Fluid Mech., **159**, 195 (1985).

Higdon, J.J.: "Effect of pressure gradients on Stokes flows over cavities", Phys. Fluids, **2**, no. 1, 112 (1990).

Jeje, A.A.: "Flows in models of microcapillaries of living plants", PhysicoChemical Hydrodynamics, **6**, no. 5-6, 647, (1985).

Lugt, H.J.: *Vortex Flow in nature and Technology*, John Wiley & Sons, NY, (1983).

Mehta, V.B. and Z. Lavan: "Flow in a two-dimensional channel with a rectangular cavity", J. of Appl. Mech., Trans. of ASME, 897, Decembe, (1969).

Pan, F. and A. Acrivos: "Steady flows in rectangular cavities", J. Fluid Mech., **28**, part 4, 643, (1967).

Payatakes, A.C., C. Tien and R.M. Turian: "Part II. Numerical solution of steady state incompressible Newtonian flow through periodically constricted tube", AIChE Journal, **19**, no.1, 67 (1973).

Roache, P.J.: *Computational Fluid Dynamics*, Hermosa Publ., New Mexico, (1976).

Salim, P.A., private communication, 1994.

Savvides, C.N. and J.H. Gerrard: "Numerical analysis of the flow through a corrugated tube with application to arterial prostheses", J. Fluid Mech., **138**, 129, (1984).

Scheidegger, A.E.: *The Physics of Flow Through Porous Media*, U. Toronto Press, Canada, 1957.

Schlichting, H.: *Boundary-Layer Theory*, McGraw-Hill Book Company, NY, (1979).

Shen C. and J.M. Floryan: "Low Reynolds number flow over cavities", Phys. Fluids, **28**, no. 11, 3191, (1985).

Sinha, S.N., A.K. Gupta and M.M. Oberai: "Laminar separating flow over backsteps and cavities. Part II. Cavities", AIAAJ, **20**, no. 3, 370, (1982).

Taylor, G.I.: "A model for the boundary condition of a porous material. Part 1", J. Fluid Mech., **49**, 319 (1971).

Vrentas, J.L., J.L. Duda and K.G. Bargeron: "Effect of axial diffuson of vorticity on flow development in circular conduit: part I. Numerical solutions", AIChEJ, **12**, 837 (1966).

Weiss, M.H.: *Drag Reduction with Riblets in Pipe Flow*, Ph.D. thesis, Mechanical Engineering Department, University of Calgary, 1993.

Wilkinson, D.L. and M.A. Willoughby: "Velocity measurement with hydrogen bubbles - the wake correction", J. Hydraulic Research, **19**, no. 2, 141, (1981).

APPENDIX A

Calibration of Differential Pressure Transducer

The Validyne DP 103 differential pressure transducer, using diaphragm dash no. 22, was calibrated using water with the display shown on Validyne CD 223 digital display. First a tygon tube manometer was attached to DP 103 and it was filled with water. Next one arm of the manometer was raised to increase the pressure and the system was allowed to come to a steady-state. After reaching steady-state, the value on the digital display was noted for the corresponding ΔP in kPa of water. In this way the whole spectrum of ΔP was covered. The pressure drop in kPa of water is plotted against the CD 223 display reading in rectangular coordinates. The calibration curve is shown in Figure A.1. A straight line is fitted through the data points using least squares method. The equation of the curve is given by,

$$\Delta P = 0.0060084 * x - 0.004814$$

where, ΔP is the pressure in kPa and x is the CD 223 display reading.

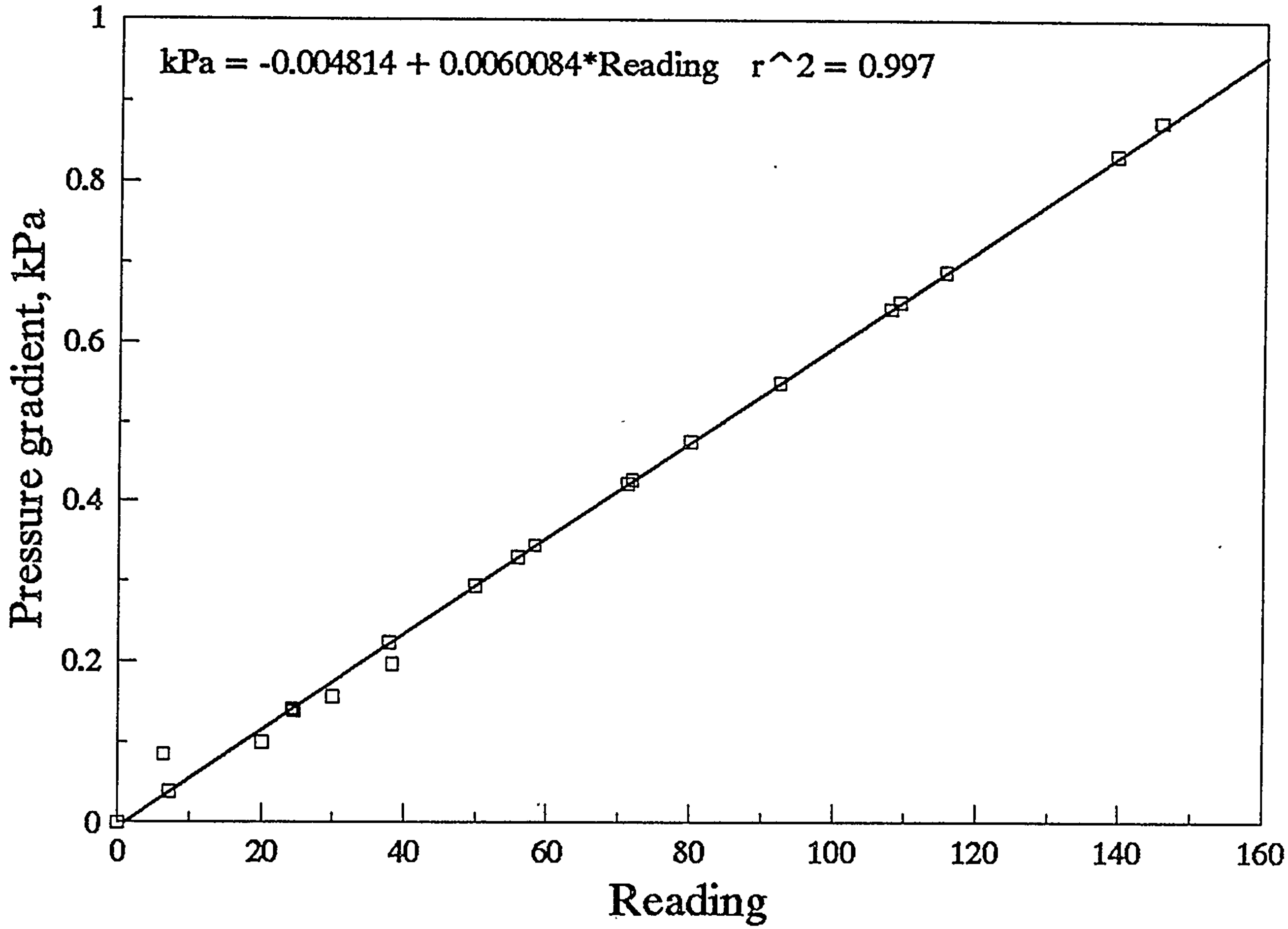

Fig.A1: Calibration of Pressure Transducer